AFRL-AFOSR-VA-TR-2019-0073

Imaging and Communication through a Combination of Turbulent and Random Discrete-Scatterer and Media

Elizabeth Bleszynski
MONOPOLE RESEARCH THOUSAND OAKS CA

03/27/2019
Final Report

Air Force Research Laboratory
AF Office Of Scientific Research (AFOSR)/ RTB1
Arlington, Virginia 22203
Air Force Materiel Command

REPORT DOCUMENTATION PAGE

Form Approved
OMB No. 0704-0188

1. REPORT DATE *(DD-MM-YYYY)*	2. REPORT TYPE	3. DATES COVERED *(From - To)*
21-03-2019	FINAL	01 Jan, 2016 - 31 Dec, 2018

4. TITLE AND SUBTITLE
Imaging and Communication through a Combination of Turbulent and Random Discrete-Scatterer Media

5a. CONTRACT NUMBER
FA9550-16-C-0014

5b. GRANT NUMBER
NA

5c. PROGRAM ELEMENT NUMBER
NA

6. AUTHOR(S)
Bleszynski, Elizabeth, H., Bleszynski, Marek, Ch., Jaroszewicz, Thomas

5d. PROJECT NUMBER
NA

5e. TASK NUMBER
NA

5f. WORK UNIT NUMBER
NA

7. PERFORMING ORGANIZATION NAME(S) AND ADDRESS(ES)
Monopole Research
739 Calle Sequoia
Thousand Oaks, CA 91360

8. PERFORMING ORGANIZATION REPORT NUMBER
MON-19-04

9. SPONSORING/MONITORING AGENCY NAME(S) AND ADDRESS(ES)
USAF, AFRL DUNS 143574726
Air Force Office of Scientific Research
875 N. Randolph Street, RM 3112
Arlington, VA 22203-1945

10. SPONSOR/MONITOR'S ACRONYM(S)
AFOSR

11. SPONSOR/MONITOR'S REPORT NUMBER(S)
NA

12. DISTRIBUTION/AVAILABILITY STATEMENT
Approved for public release, distribution is unlimited.

13. SUPPLEMENTARY NOTES
The views, opinions and/or findings contained in this report are those of the author(s) and should not be construed as an official Department of the Air Force position, policy or decision, unless so designated by other documentation.

14. ABSTRACT
The principal goal of our project was to develop a formulation for pulse forming, detection, and processing methods which would enhance signal penetration through obscuring media, without compromising the range resolution in imaging and/or the bit rate in communication. The main idea was to utilize incoherently detected pulses (through measurements of their intensity). The underlying approach was based on analytic complex-contour integration of numerically determined cut and pole singularities of the radiative transport equation solution in the Fourier space. The approach allows to take advantage of the reduced pulse attenuation and reduce the detrimental effects of diffusion by means of processing of the received signal.

15. SUBJECT TERMS
discrete-scatterer media, aerosol and cloud effects, diffusion, early-time diffusion, enhaced signal penetration, radiative transport, point spread function, modulation transfer function, forward scattering, multiple scattering, deblurring, surface and volume integral equation, singularity extraction, non-singular laplacian representation

16. SECURITY CLASSIFICATION OF:			17. LIMITATION OF ABSTRACT	18. NUMBER OF PAGES	19a. NAME OF RESPONSIBLE PERSON
a. REPORT	b. ABSTRACT	c. THIS PAGE			Elizabeth Bleszynski
					19b. TELEPHONE NUMBER *(Include area code)*
unclassified	unclassified	unclassified	UU	35	805 375-0318

Contents

1 Objectives

Imaging and communication with optical or infrared pulsed signals through obscuring random media (e.g., atmospheric clouds, fog, dust, or aerosols) is a long-standing and challenging problem, both experimentally and theoretically.

From the experimental and applications perspective, a *coherently* detected pulse field preserves its time profile, but is strongly attenuated, at the rate proportional to the total cross-section of the wave on an individual medium scatterer. The *incoherently* detected field intensity, although attenuated at a lower rate (proportional to the absorption cross-section), spreads in transverse directions and develops a long diffusive temporal tail, which causes loss of resolution in imaging and loss of bandwidth in communication.

The principal goal of our project was to develop a formulation for pulse forming, detection, and processing methods which would *enhance signal penetration through obscuring media, without compromising the range resolution in imaging and/or the bit rate in communication.*

The main idea was to utilize *incoherently detected pulses* (through measurements of their *intensity*). The underlying approach was based on analytic complex-contour integration of numerically determined cut and pole singularities of the radiative transport equation solution in the Fourier space. Such an approach allows to take advantage of the reduced pulse attenuation and, at the same time, reduce the detrimental effects of diffusion by means of processing of the received signal.

2 Summary of the results

We developed rigorous approach [1] based on analytic complex-contour integration of numerically determined cut and pole singularities of the radiative transport equation solution in the Fourier space. We found, in the context of simulations based on the developed algorithm, that the intensity of an optical pulse propagating in a dilute random medium composed of scatterers large compared to the pulse carrier wavelength (a condition well-met in the atmospheric cloud propagation scenario) contains, in addition to the coherent ("ballistic") contribution and a long late-time diffusive tail, a *narrow, sharply rising early-time diffusive component* which

- can be attributed to the small-angle diffractive part of the scattering cross-section on individual medium particles,
- is attenuated proportionally to the non-diffractive rather than total cross-section,
- can be extracted (due to its sharp rise and therefore rich high frequency content) by high-pass filtering of the received pulse , i.e., without the necessity of performing any of the time-gating procedures,

In what follows we describe the areas of our work and our main results.

2.1 Enhancing the strength of the early-time diffusion signal through beam collimation in pulse propagation in sparse discrete random media.

Propagation of short infrared/optical pulses in dilute random media (e.g., atmospheric clouds, fog, dust, or aerosols) consisting of large, compared to the wavelength, scatterers, was analyzed in the framework of the radiative transport equation (RTE).

An emphasis was put on investigating properties of the RTE eigenmodes. It was found that, in addition to the modes characterized by smooth angular distributions of the energy flux density and responsible for the conventional "late-time" diffusion, there exists another class of modes, exhibiting collimated angular distributions and giving rise to the previously identified early-time diffusion phenomenon – a sharply rising structure in the time-resolved intensity, immediately following the coherent signal, but attenuated at a lower rate.

It was shown that designing a source strongly coupled to the collimated modes significantly enhances the early-time diffusion signal and thus increases its potential usefulness in imaging and communication.

The approach is described in detail in [2]. The paper is attached to this report as Appendix A.

2.2 Improving resolution in imaging through obscuring media with early-time diffusion signals

We extended the analysis of early-time diffusion (ETD) phenomenon to the description of an imaging scenario involving a two-way (from the source to the observed object and back to the detector) propagation of a short pulse through a layer of an obscuring random medium.

We carried out a detailed analysis of the angular distributions of the energy flux in solutions of the time-dependent RTE, resulting in computation of the point-spread function (PSF) based on the extracted ETD component of the image.

The obtained PSF and the corresponding modulation transfer function (MTF) characterizes both the incoherent ETD contribution (i.e., lower Fourier components of the PSF) and the quasi-coherent ETD contribution (the highest Fourier components), as well as the important transition between the two regions. The computation, which included very high angular momenta ($l > 1000$), was facilitated by development of a novel analytic technique allowing efficient transformation between angular momenta in the RTE solution and the Fourier components of the PSF.

We showed that the angular resolution implied by the computed PSF is controlled by the behavior of the dominant RTE modes responsible for the ETD signal and is comparable to the angular width of the scattering cross-section on an average medium constituent.

Subsequently, we developed a regularized-deconvolution technique which allowed a *further significant resolution improvement* - typically by the factor of 3 or 4 for propagation at the distance of about 20 mean free paths - by enhancing higher Fourier components of the PSF, up to the highest ϱ values for which the radiance is still attenuated at a reduced rate.

Development a regularized-deconvolution technique is an important result which may further enhance the prospects of application of the ETD phenomenon in imaging.

The approach and the results are described in detail

- in the paper entitled "Improving resolution in imaging through obscuring media with early-time diffusion signals"; the paper was submitted for publication to the Journal of the Optical Society of America A and is attached to this report as Appendix B,

- in the invited conference contribution "Early-time diffusion in imaging through obscuring random media - two-way propagation and deblurring", ICEAA 2018, attached here as Appendix C.

2.3 A novel and efficient procedure for the evaluation of matrix elements of the tensor and vector Green functions in volumetric and surface integral equations in electromagnetics

As a tool useful in numerical verification of some aspects the RTE, a novel procedure was developed [3, 4] for the evaluation of matrix elements of the tensor Green function with Rao-Wilton-Glisson basis functions (defined on triangular supports) appearing in surface integral equations and Schaubert-Wilton-Glisson basis functions (defined on tetrahedral supports) appearing in volume integral equations in electromagnetics.

The procedure is based on evaluating Galerkin matrix elements of electromagnetic volume and surface integral equations with the help of suitably constructed Laplacian-type representations of singular kernels (Green functions) in terms of non-singular auxiliary functions.

The task of finding specific Laplacian representations of various kernels amounts to solving appropriate ordinary or partial inhomogeneous differential equations. Simple solutions of resulting ordinary differential equations which pertain to volume and planar surface geometries are obtained in terms of elementary functions. In the case of basis functions supported on non-parallel surface elements, partial differential equations for the auxiliary functions are first solved in Fourier space and then transformed to simple expressions in coordinate space by evaluating integrals similar to those used in treating Feynman diagrams.

The properly chosen Laplacian representations allow us, by using the Gauss divergence theorem, to convert volumetric and surface integrals representing matrix

elements to respective surface or line integrals always involving only non-singular integrands.

The main advantage of the derived expressions is that they offer simplicity and easily controllable accuracy achieved at a computational cost significantly lower than that the for previously considered techniques, in particular the conventional singularity subtraction method.

The invited 2017 EUCAP Symposium [5] and 2018 International Workshop on Computing, Electromagnetics, and Machine Intelligence, CEMi'18 contributions addressing the above developments are attached as Appendices D and E.

3 Publications resulting from Grant # FA9550-16-C-0014

E. Bleszynski, M. Bleszynski, and T. Jaroszewicz, "Enhancing early-time diffusion through beam collimation in pulse propagation in sparse discrete random media," Optics Letters, vol. 43, no. 15, pp. 3762-3765, 2018.

E. Bleszynski, M. Bleszynski, and T. Jaroszewicz, "Improving resolution in imaging through obscuring media with early-time diffusion signals", submitted for publication in the Journal of the Optical Society of America A.

E. Bleszynski, M. Bleszynski, and T. Jaroszewicz, "Reduction of singular surface integrals to nonsingular line integrals in integral equations for planar geometries," IEEE Transactions on Antennas and Propagation, vol. 64, no. 11, pp. 4760-4769, 2016.

E. Bleszynski, M. Bleszynski, and T. Jaroszewicz, "Reduction of singular surface integrals to non-singular line integrals in integral equations involving non-parallel surface elements," in 2017 11th European Conference on Antennas and Propagation (EUCAP), pp. 303-307, IEEE, 2017

References

[1] E. Bleszynski, M. Bleszynski, and T. Jaroszewicz, "Early-time diffusion in pulse propagation through dilute random media," *Optics Letters*, vol. 39, no. 20, pp. 5862–5865, 2014.

[2] E. Bleszynski, M. Bleszynski, and T. Jaroszewicz, "Enhancing early-time diffusion through beam collimation in pulse propagation in sparse discrete random media," *Optics Letters*, vol. 43, no. 15, pp. 3762–3765, 2018.

[3] E. H. Bleszynski, M. K. Bleszynski, and T. Jaroszewicz, "Reduction of volume integrals to nonsingular surface integrals for matrix elements of tensor and vector Green functions of Maxwell equations," *IEEE Transactions on Antennas and Propagation*, vol. 61, pp. 3642–3647, 2013.

[4] E. H. Bleszynski, M. K. Bleszynski, and T. Jaroszewicz, "Reduction of singular surface integrals to nonsingular line integrals in integral equations for planar geometries," *IEEE Transactions on Antennas and Propagation*, vol. 64, no. 11, pp. 4760–4769, 2016.

[5] E. Bleszynski, M. Bleszynski, and T. Jaroszewicz, "Reduction of singular surface integrals to non-singular line integrals in integral equations involving non-parallel surface elements," in *2017 11th European Conference on Antennas and Propagation (EUCAP)*, pp. 303–307, IEEE, 2017.

Optics Letters

Enhancing early-time diffusion through beam collimation in pulse propagation in sparse discrete random media

ELIZABETH BLESZYNSKI,* MAREK BLESZYNSKI, AND THOMAS JAROSZEWICZ

Monopole Research, Thousand Oaks, California 91360, USA
**Corresponding author: elizabeth@monopoleresearch.com*

Received 17 May 2018; accepted 26 June 2018; posted 6 July 2018 (Doc. ID 331789); published 1 August 2018

Solutions of the time-dependent radiative transfer equation (RTE) are used to describe propagation of a pulsed collimated beam through a random medium consisting of discrete scatterers of sizes large compared to the wavelengths—a situation particularly relevant to free-space optical communication through atmospheric obscurants. The RTE is solved in the spherical-harmonics basis with no approximations other than a truncation N in the angular momenta; the results confirm convergence of the solution for a fixed beam width and growing N. The obtained time-resolved radiance includes both the usual "late-time diffusion" (LTD), responsible for the well known reduction of the "coherence bandwidth" and, thus, a serious limitation in the transfer rate, and the more recently identified "early-time diffusion" (ETD) component, attenuated at a rate significantly lower than for the coherent (ballistic) signal and characterized by a very short rise time, allowing a high-rate data transfer. The ratio of the ETD to the LTD signal for the considered collimated beams is much (orders of magnitude) higher than in the previously examined problem of an omnidirectional source, increasing its potential usefulness in communication and related imaging applications.

OCIS codes: (030.5620) Radiative transfer; (290.1090) Aerosol and cloud effects; (290.1990) Diffusion; (290.2558) Forward scattering; (070.2615) Frequency filtering.

https://doi.org/10.1364/OL.43.003762

In comparison with optical fiber and microwave communication, free-space optical (FSO) communication with short pulses offers, potentially, multiple advantages—especially a low cost of deployment and a high bit rate. Nevertheless, scattering in atmospheric media (haze, fog, clouds, rain) remains a major problem, causing both losses and a reduction in the data rate [1]. The latter difficulty is believed to be due to temporal spreading of propagating pulses caused by scattering-induced diffusion [2–5], as described by the radiative transfer equation (RTE) [6–9].

The commonly invoked physical picture is that a pulse propagating in a scattering medium contains a short but strongly attenuated coherent (ballistic) component and a slowly decaying "late-time diffusion" (LTD) tail, whose length grows with the propagation distance R as $\Delta t_{\mathrm{LTD}} \sim R^2/(v_0 \ell_{\mathrm{t}})$, where $v_0 \approx c$ is the coherent wave propagation speed, and ℓ_{t} is the mean-free-path in the medium (typically, several tens of meters for an optical pulse traveling in an atmospheric cloud or fog). The time Δt may easily exceed a microsecond scale, resulting in the "coherence bandwidth" [2–4] of the order 1 MHz and the correspondingly limited bit rate.

However, it has been noticed [10] that, if the scatterers in the medium are sizable compared to the signal wavelength, $2\pi a \gg \lambda_0$, the time-dependent RTE solutions develop an additional "early-time diffusion" (ETD) component immediately following the ballistic one. This component is due to multiple small-angle scattering within the forward-scattering peak of the medium constituent differential cross-section and is characterized by a rise time

$$\Delta t_{\mathrm{ETD}} \approx \frac{\kappa}{(k_0 a)^2} \frac{R^2}{v_0 \ell_{\mathrm{t}}}, \tag{1}$$

where $k_0 = 2\pi/\lambda_0$ is the pulse center wave number, a is the scatterer radius, and, empirically, $\kappa \lesssim 0.1$. Since in typical atmospheric propagation scenarios $k_0 a$ may be large (say, ~50), the time Δt_{ETD} may be several orders of magnitude shorter than the LTD time scale. Therefore, the rapidly rising ETD signal, isolated by means of high-pass filtering, may be potentially used in communication with a much higher data rate than would be allowed by the LTD mechanism. Equally importantly, the EDT component is attenuated at a rate significantly reduced compared to that of the coherent signal (about 0.65 for visible light propagating in an atmospheric cloud or fog [10]).

The existence of the ETD phenomenon has been originally established and discussed [10] in the case of an omnidirectional source, which is relevant in describing light reflection from diffusively scattering objects, but not adequate in the context of communication (and many types of imaging) relying on narrowly collimated beams. In this Letter, we address the behavior of the ETD component in the latter problem and discuss its specific features—not apparent in the previously described solutions, but necessary in order to model propagation of narrow beams—primarily, the angular distribution of the energy flux.

We note that, while previous treatments of RTE for collimated scattering were based on small-angle, parabolic-type

approximations, our approach is the first one, to the best of our knowledge, in which the time-dependent RTE for *large scatterers* is solved with no approximations other than a truncation in the spherical-harmonics expansion; we show the convergence of the results with the increasing truncation parameter. The unique feature of our approach is that it correctly describes the full range of angular momenta from *low values responsible for the LTD behavior* to *high values associated with the ETD*, and its *transition to the coherent (ballistic) regime*.

We model pulse propagation in an infinite random-scatterer medium by means of the integro-differential scalar RTE,

$$(\mu_t + v_0^{-1}\partial_t + \hat{\boldsymbol{s}}\cdot\nabla_{\boldsymbol{R}})\Gamma(t,\boldsymbol{R};\hat{\boldsymbol{s}},\hat{\boldsymbol{s}}') - \int \mathrm{d}^2\hat{s}''\Sigma(\hat{\boldsymbol{s}}\cdot\hat{\boldsymbol{s}}'')\Gamma(t,\boldsymbol{R};\hat{\boldsymbol{s}}'',\hat{\boldsymbol{s}}') = \delta(t)\delta^3(\boldsymbol{R})\delta^2(\hat{\boldsymbol{s}}-\hat{\boldsymbol{s}}') \quad (2)$$

for the Green function representing the probability density of an infinitely short light pulse emitted in the direction $\hat{\boldsymbol{s}}'$ at the time 0 from a source at $\boldsymbol{0}$ to arrive in the direction $\hat{\boldsymbol{s}}$ at the time t at the observation point $\boldsymbol{R}$. The coherent attenuation coefficient (the inverse of the mean-free-path) is $\mu_t = 1/\ell_t = n_0\sigma_t$, where n_0 is the medium number density, and σ_t is the ensemble-averaged total cross-section on a single scatterer; in the scattering kernel $\Sigma(x) = n_0\sigma(x)$, $\sigma(x)$ is the corresponding differential cross-section ensemble-averaged over scatterer sizes, shapes, orientations, dielectric properties, etc., and, therefore, dependent only on x, the cosine of the scattering angle.

We solve the RTE in Eq. (2) by means of the standard Green function expansion in plane waves in the variables t and $\boldsymbol{R}$ and in spherical harmonics [7] or, more conveniently, in rotated spherical harmonics [11–13] in the variables $\hat{\boldsymbol{s}}$ and $\hat{\boldsymbol{s}}'$. After projecting on the same basis and truncating to $l, l' < N$, one obtains for $t > 0$ the solution

$$\Gamma(t,\boldsymbol{R};\hat{\boldsymbol{s}},\hat{\boldsymbol{s}}') = v_0\sum_m\sum_j\int\frac{\mathrm{d}^3P}{(2\pi)^3}\mathrm{e}^{-\mathrm{i}\Omega_j^m(P)t}\mathrm{e}^{\mathrm{i}\boldsymbol{P}\cdot\boldsymbol{R}} \times\sum_{l,l'}w_{j,l}^m(P)w_{j,l'}^m(P)Y_{l,m}(\hat{\boldsymbol{s}};\hat{\boldsymbol{P}})Y_{l',m}^*(\hat{\boldsymbol{s}}';\hat{\boldsymbol{P}}), \quad (3)$$

where $Y_{l,m}(\hat{\boldsymbol{s}};\hat{\boldsymbol{P}})$ is the rotated spherical harmonic defined relative to the direction $\hat{\boldsymbol{P}}$, and $j = 1, 2, \ldots, (N-|m|)^2$ labels normalized (to $w_j^m(P)^T w_j^m(P) = 1$) eigenvectors, obtained by solving the eigenequation

$$M^m(P)w_j^m(P) = \mathrm{i}v_0^{-1}\Omega_j^m(P)w_j^m(P). \quad (4)$$

Here, the complex symmetric $(N-|m|)\times(N-|m|)$ matrix $M^m(P)$ has elements $M_{l,l'}^m(P) = (\mu_t - \Sigma_l)\delta_{l,l'} + iP(\delta_{l,l'+1}b_l^m + \delta_{l',l+1}b_{l'}^m)$ with $b_l^m = [(l^2-m^2)/(4l^2-1)]^{1/2}$ and the coefficients $\Sigma_l = 2\pi\int_{-1}^{1}\mathrm{d}xP_l(x)\Sigma(x)$, proportional to projections of the scattering cross-section on Legendre polynomials.

In the following, we consider an axisymmetric problem with a spatially small source located at the origin, emitting a pulsed beam in the z direction. For simplicity, we assume a factorized source distribution $S(t,\hat{\boldsymbol{s}}) = A(t)B_\Theta(\hat{\boldsymbol{z}}\cdot\hat{\boldsymbol{s}})$ with $A(t)$ representing a short pulse (defined below) and with a Gaussian-type beam shape

$$B_\Theta(\hat{\boldsymbol{z}}\cdot\hat{\boldsymbol{s}}) = \frac{1}{2\pi\Theta^2}\mathrm{e}^{-(1-\hat{\boldsymbol{z}}\cdot\hat{\boldsymbol{s}})/\Theta^2} \quad (5)$$

of angular width $\Theta \ll 1$. The time-resolved intensity at an observation point $\boldsymbol{R} = R\hat{\boldsymbol{z}}$ on the beam axis is then given by the convolution of the Green function with the source temporal and angular distribution $S(t',\hat{\boldsymbol{s}}')$, integrated over all arriving flux directions $\hat{\boldsymbol{s}}$,

$$I_\Theta(t,R) = \int\mathrm{d}t'\int\mathrm{d}^2\hat{s}\int\mathrm{d}^2\hat{s}'\Gamma(t-t',R\hat{\boldsymbol{z}};\hat{\boldsymbol{s}},\hat{\boldsymbol{s}}')S(t',\hat{\boldsymbol{s}}'). \quad (6)$$

With the Green function of Eq. (3), the intensity of Eq. (6) takes the form

$$I_\Theta(t,R) = \sum_{l=0}^{\infty}\sqrt{2l+1}\,C_l(\Theta)\mathrm{J}_l(t,R). \quad (7)$$

Here, the partial-wave intensities J_l are expressed in terms of the eigenvectors $w_j^m(P)$ defined by Eq. (4):

$$\mathrm{J}_l(t,R) = \frac{v_0}{2\pi^2}\int\mathrm{d}t'\int_0^\infty\mathrm{d}PP^2\sum_j\mathrm{e}^{-\mathrm{i}\Omega_j^0(P)(t-t')}i^l\mathrm{j}_l(PR) \times w_{j,0}^0(P)w_{j,l}^0(P)A(t') \quad (8)$$

(because of the axial symmetry, only $m = 0$ modes contribute here), and {[14], Eq. (2.17.5.2)}

$$C_l(\Theta) = \int\mathrm{d}^2\hat{s}P_l(\hat{\boldsymbol{z}}\cdot\hat{\boldsymbol{s}})B_\Theta(\hat{\boldsymbol{z}}\cdot\hat{\boldsymbol{s}}) = \frac{2}{\Theta^2}\mathrm{e}^{-1/\Theta^2}\mathrm{i}_l\left(\frac{1}{\Theta^2}\right), \quad (9)$$

where $\mathrm{i}_l(x) \equiv \mathrm{i}_l^{(1)}(x)$ are modified spherical Bessel functions {[15], Eq. (10.47.7)}. For $\Theta \ll 1$, the coefficients of Eq. (9) are very accurately approximated by $\exp(-\Theta^2 l^2/2)$.

As an example, we consider the RTE solution for an optical pulse (center wavelength of $\lambda_0 = 0.633$ μm) propagating in an atmospheric cloud or fog consisting of spherical water droplets (relative permittivity $\epsilon = 1.77$) of radii following the gamma distribution with the conventional shape parameter $\nu = 10$ and with the average radius $a = 5$ μm $\approx 7.9\,\lambda_0$, hence, $k_0 a \approx 50$. Such droplets are characterized by a strongly forward-peaked Mie-scattering differential cross-section. The assumed number density $n_0 = 10^{-9}$ m^{-3} yields the attenuation coefficient $\mu_t = 1/\ell_t \approx (6\text{ m})^{-1}$.

We also assume a Gaussian pulse $A(t) = \exp(-t^2/2T_p^2)/(\sqrt{2\pi}T_p)$ of duration $T_p = 0.003\ell_t/v_0 = 60$ ps, less than the ETD time scale of Eq. (1), which, in the present case and for the considered propagation distances (up to $R = 24\ell_t$), is $\Delta t_{\mathrm{ETD}} \lesssim 0.010\ell_t/v_0 = 200$ ps. This finite pulse width introduces an effective cutoff in the P integral of Eq. (8).

The RTE spectrum can be well characterized by considering just the attenuation coefficients

$$\mu_j^m(P) = -\mathrm{Im}\,\Omega_j^m(P)/v_0, \quad (10)$$

plotted in Fig. 1 for a particular truncation $N = 800$. Obviously, for any finite truncation N, the spectrum is purely discrete. However, the plots indicate that the spectrum can be, approximately, split into the "quasi-continuum" and "truly discrete" subsets:

(i) In the quasi-continuum spectrum, the attenuation coefficient values form a densely populated band $\mu_j^0(P)/\mu_t \approx 1$, i.e., at the level of the coherent wave attenuation. The corresponding velocity eigenvalues $v_j^m(P) = \mathrm{Re}\,\Omega_j^m(P)/P$ are uniformly distributed over the interval $[-v_0, v_0]$.

(ii) The discrete frequency eigenvalues persist only up to a certain critical P value [16] $P_{\max} \sim (k_0 a)^2\mu_t$. Their "level density" is low for small $\mu_j^0(P)/\mu_t$ and increases on approaching the quasi-continuum $\mu_j^0(P)/\mu_t \approx 1$.

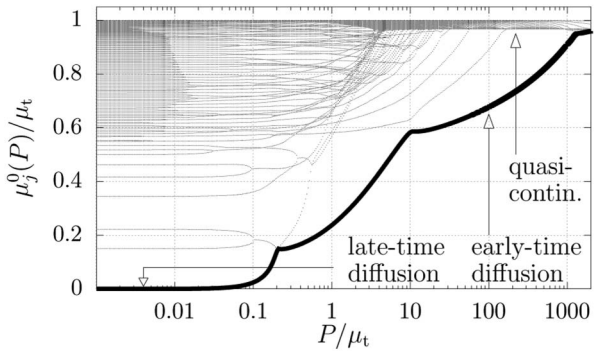

Fig. 1. Radiance attenuation coefficients of Eq. (10), relative to the coherent attenuation coefficient μ_t. The thick solid line marks the "leading trajectory" consisting of the least attenuated modes.

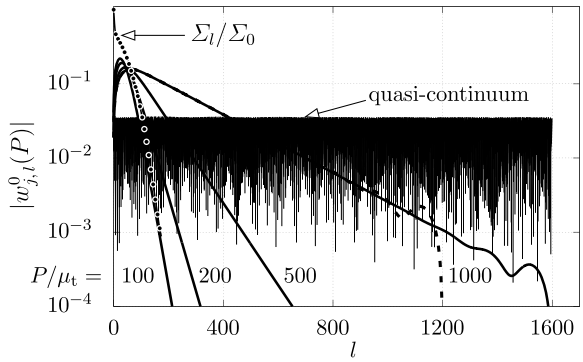

Fig. 2. l components of the eigenvector $w_j^0(P)$ dominant for a given P for several values of P: $P/\mu_t = 100, 200, 500, 1000$ for $N = 1600$ (thick solid lines) and $N = 1200$ (thick dashed line). The thin lines show components of typical quasi-continuum eigenvectors.

By comparing solutions for different N, one can see that as N increases new modes are added to the quasi-continuum band (whose width shrinks proportionally to $1/N$), while the discrete eigenvalues approach their asymptotic $N = \infty$ locations. In the exact (not truncated) RTE, the continuum spectrum is $\Omega \in [v_0(-P - i\mu_t), v_0(P - i\mu_t)]$ and the discrete-spectrum eigenvalues are contained in the region $-v_0 P \le \mathrm{Re}\,\Omega \le v_0 P$, $\mathrm{Im}\,\Omega \le 0$, as can be deduced from the integral form of the RTE.

In the previously considered [10] omnidirectional source problem, the behavior of the time-resolved intensity could be explained almost entirely in terms of the frequency eigenvalue distributions: the coefficient $J_0(t, R)$ involves only the $l = 0$ components of the normalized eigenvectors w_j^0, which have relatively weak dependence on P and j. In this case, the sum in Eq. (8) is dominated for every P by the "leading" mode, i.e., that having the lowest attenuation coefficient of Eq. (10). Those modes form a "leading trajectory" of eigenvalues, marked by a thick line in Fig. 1. Its low attenuation for $P/\mu_t \lesssim 0.1$ is characteristic of the usual LTD; with growing P, its attenuation increases but, up to $P = P_{\max} \approx 1500\mu_t$, remains lower than the coherent attenuation and gives rise to the ETD signal. The corresponding velocities (not plotted) are nearly zero and nearly v_0 in the LTD and ETD regions.

In the present problem of a *collimated* beam, high-l components in Eq. (7) become essential, and the distribution of the eigenvector components becomes as important as the behavior of eigenvalues. In Fig. 2, we plot such distributions for four high P values ($P/\mu_t = 100, 200, 500, 1000$) responsible for the ETD phenomenon [for low P, all discrete-spectrum eigenvectors have a very narrow l distributions and contribute mostly to the $l = 0$ term in Eq. (7)]. For each of the four P values, we selected here the leading (least attenuated) discrete-spectrum mode and one mode belonging to the quasi-continuum. [As a rule, nonleading discrete-spectrum modes have narrow l distributions and thus a minor effect on the large-l behavior of the partial-wave intensities in Eq. (7).] For the lowest considered value of $P = 100\mu_t$, the l distribution of the discrete-spectrum eigenvector elements is similar to that of the cross-section coefficients Σ_l, also plotted for comparison. With increasing P, the l distributions of the eigenvectors significantly widen, corresponding to narrowing of the angular distributions of the eigenfunctions. In contrast, quasi-continuum eigenvectors have for *all* P values very wide l distributions with comparable components in the entire range $0 \le l < N$. The solutions were computed here with the truncation $N = 1600$, which is seen to have an effect only for l fairly close to N, as confirmed by an additional curve obtained with $N = 1200$.

The computed spectrum and eigenvectors constitute the basis for evaluating the partial-wave intensities $\mathrm{J}_l(t, R)$ and the observed intensity $I_\Theta(t, R)$ of Eq. (7). In particular, distributions of the eigenvectors' components $w_{j,l}^0$ control, through Eq. (8), the l dependence of the intensities $\mathrm{J}_l(t, R)$.

To visualize the behavior of the terms in Eq. (7), we plot in Fig. 3 the factors $C_l(\Theta)$ and time averages

$$\langle \mathrm{J}_l(\cdot, R)\rangle = (t_2 - t_1)^{-1} \int_{t_1}^{t_2} \mathrm{d}t \mathrm{J}_l(t, R) \qquad (11)$$

of the partial-wave intensitites of Eq. (8) taken over the interval defined by $(v_0 t_1 - R)/\ell_t = -0.01$ and $(v_0 t_2 - R)/\ell_t = 0.05$, in which the ETD signal is concentrated (cf. Fig. 4). Here and in Fig. 4, the time-resolved intensities are plotted in the units of v_0/ℓ_t^3.

Since the factors $C_l(\Theta)$ decay very rapidly with l, only a limited range of l values contributes for a given value of Θ, and the RTE may be safely truncated at, say, $N = 6/\Theta$, corresponding to $C_l(\Theta) < 10^{-7}$. Figure 3 shows perfect stability of the averages $\langle \mathrm{J}_l(\cdot, R)\rangle$ for fixed l and increasing N and

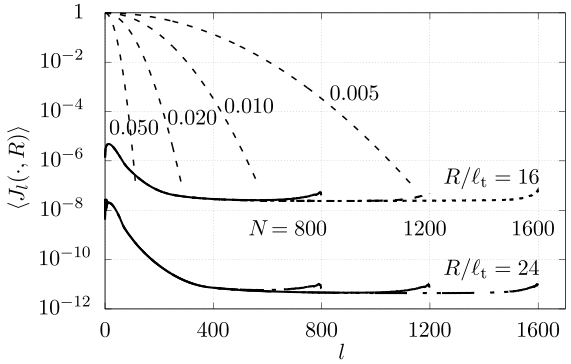

Fig. 3. Time-averages $\langle \mathrm{J}_l(\cdot, R)\rangle$ of the partial-wave intensities for two propagation distances and for several truncations N as functions of l (solid curves). The dashed curves represent the factors $C_l(\Theta)$ for the indicated beam widths $\Theta = 0.050, 0.020, 0.010, 0.005$.

provides a practical "numerical proof" of the convergence of the solutions.

Figures 2 and 3 illustrate several important facts:

1. For large l, the coefficients $\langle \mathrm{J}_l(\cdot, R)\rangle$ approach constant values, resulting from the quasi-continuum modes of Fig. 2. It can be shown that, in fact, those coefficients converge to the values of the "coherent" contribution to the radiance, *defined* as the solution of the RTE without the scattering kernel ($\Sigma \equiv 0$).
2. At smaller l, the enhancement of $\langle \mathrm{J}_l(\cdot, R)\rangle$ above its "coherent" level is due to contributions of the discrete modes represented in Fig. 2. This enhancement is precisely the ETD signal characterized by the l range $\sim k_0 a$ (here about 50), but decreasing with l rather slowly and still having a significant effect even at $l \sim 300$. Thus, Fig. 3 shows a gradual transition between the incoherent ETD radiance behavior in the smaller l region and its asymptotic "coherent" large-l limit.
3. As functions of R, the factors $\langle \mathrm{J}_l(\cdot, R)\rangle$ decay at different rates in various l ranges. In the high-l regime, their decay $\sim \exp(-\mu_t R)$ is controlled by the coherent wave attenuation, while for low l, their attenuation rate is reduced to about $0.65\mu_t$, the factor 0.65 being the ratio of the "nondiffractive" scattering cross-section (i.e., that outside the forward "diffractive" scattering peak) to the total cross-section [10].

Finally, the top plot in Fig. 4 depicts the early-time (first 8 ns) behavior of the time-resolved intensities $I_\Theta(t, R)$. They are computed according to Eq. (6) for propagation distance $R = 24\ell_t$ (i.e., $R \approx 144$ m in the considered atmospheric cloud medium) and for several angular beam widths Θ. The ETD signal persists over the time interval of approximately 1 ns, while, as the time increases, formation of the LTD signal becomes visible. The bottom plot in that figure shows the same intensities after high-pass filtering, which isolates the ETD component of the signal, characterized by a short rise-time. We used here a Gaussian filter $1 - \exp(-T_f^2\Omega^2/2)$, as described in Ref. [10], assuming the filter width $T_f = 0.010\ell_t/v_0 = 200$ ps, about three times wider than the emitted pulse. The time-resolved intensities for the omnidirectional source (multiplied by 100 and 300) are included for comparison.

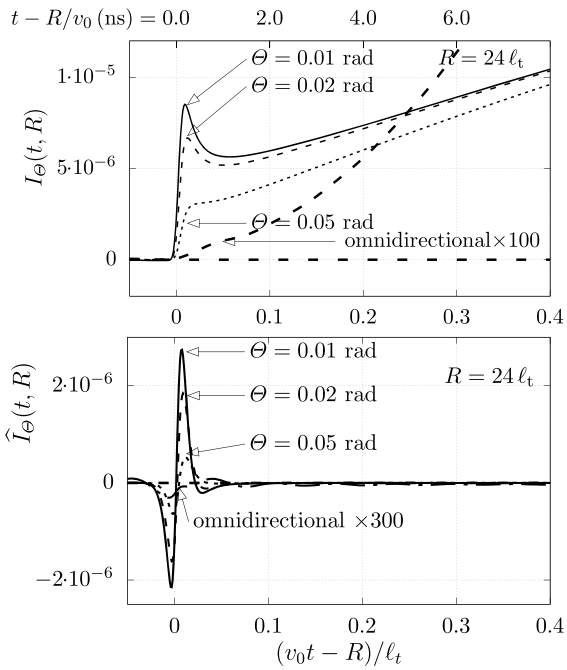

Fig. 4. Time-resolved field intensities at the distance $R = 24\ell_t$ calculated for an omnidirectional source and for sources with different angular widths Θ: received intensity (top) and high-pass filtered (bottom). The parameters are given in the text.

The curves in Fig. 4 demonstrate that the magnitude of the ETD signal significantly increases with the decreasing angular width of the source distribution Θ. In particular, as soon as Θ becomes comparable to or smaller than Θ_σ (the width of the forward-scattering peak of the angular cross-section on an average medium constituent, here ≈0.021 rad), the ETD signal becomes at least three orders of magnitude stronger than that due to the omnidirectional source. Physically, at this degree of beam collimation, the source injects most of its energy into the desired ETD eigenmodes (which have comparable angular widths), whereas for an omnidirectional source only its small fraction $\sim\Theta_\sigma^2$ can be utilized.

Although we concentrated here on optical communication applications, our results can be also directly utilized (with an appropriate change of scales) in millimeter-wave pulse propagation through precipitation. They can also be used in many types of transmission (trans-illumination) imaging, including biomedical imaging or combustion diagnostics. On the other hand, reflection-type imaging applications, involving two-way propagation, require a more extensive analysis, which will be presented elsewhere.

Funding. Air Force Office of Scientific Research (AFOSR) (FA 9550-16-C-0014).

REFERENCES AND NOTE

1. M. A. Khalighi and M. Uysal, IEEE Commun. Surveys Tuts. **16**, 2231 (2014).
2. A. Ishimaru and S. T. Hong, Radio Sci. **10**, 637 (1975).
3. S. T. Hong and A. Ishimaru, Radio Sci. **11**, 551 (1976).
4. S. Hong, I. Sreenivashiah, and A. Ishimaru, IEEE Trans. Antenas Propag. **25**, 822 (1977).
5. A. D. Kim, A. Ishimaru, and Y. Kuga, Proc. SPIE **3609**, 101 (1999).
6. S. Chandrasekhar, *Radiative Transfer* (Dover, 1960).
7. K. M. Case and P. F. Zweifel, *Linear Transport Theory*, Addison-Wesley Series in Nuclear Science and Engineering (Addison-Wesley, 1967).
8. A. Ishimaru, *Wave Propagation and Scattering in Random Media* (Wiley, 1999).
9. L. Ryzhik, G. Papanicolaou, and J. B. Keller, Wave Motion **24**, 327 (1996).
10. E. Bleszynski, M. Bleszynski, and T. Jaroszewicz, Opt. Lett. **39**, 5862 (2014).
11. V. A. Markel, Waves Random Media **14**, L13 (2004).
12. G. Panasyuk, J. C. Schotland, and V. A. Markel, J. Phys. A **39**, 115 (2006).
13. A. Liemert and A. Kienle, Phys. Rev. E **86**, 036603 (2012).
14. A. P. Prudnikov, Y. A. Brychkov, and O. I. Marichev, *Integrals and Series. Vol. 2: Special Functions* (Gordon and Breach, 1986).
15. F. W. J. Olver, D. W. Lozier, R. F. Boisvert, and C. W. Clark, eds., *NIST Handbook of Mathematical Functions* (Cambridge University, 2010).
16. The absence of the discrete spectrum for sufficiently high P can be intuitively explained [10] by an approximate relation of the RTE to a Schrödinger equation with the potential proportional to Σ/P: for a weak potential, there are no discrete energy levels (bounds states).

APPENDIX B (SUBMITTED TO JOSA A)

Improving resolution in imaging through obscuring media with early-time diffusion signals

ELIZABETH BLESZYNSKI[1*], MAREK BLESZYNSKI[1], AND THOMAS JAROSZEWICZ[1]

[1] *Monopole Research, Thousand Oaks CA, 91360*
[*] *Corresponding author: elizabeth@monopoleresearch.com*

Compiled March 21, 2019

A short pulse propagating through a medium consisting of randomly distributed scatterers, large compared to the wavelength, is expected to develop an "early-time diffusion" (ETD) behavior: a sharply rising structure in the time-resolved intensity, immediately following the coherent (ballistic) component. Since the ETD signal is attenuated at a rate substantially lower than the coherent wave, it offers a possibility of application in imaging through scattering media (e.g., atmospheric obscurants). We describe here imaging scenarios utilizing the ETD phenomenon, examine image formation techniques, and evaluate, by using the radiative transport theory, the resulting point-spread function (PSF) characterizing the image resolution. A directly formed image is shown to have an angular resolution comparable to the width of the forward peak in the scattering cross-section of the medium constituents. This resolution can be significantly improved by enhancing higher Fourier components of the PSF by means of regularized deconvolution techniques.

OCIS codes: (030.5620) Radiative transfer, (290.1090) Aerosol and cloud effects, (290.1990) Diffusion, (290.2558) Forward scattering, (290.4210) Multiple scattering, (110.4100) Modulation transfer function, (100.1830) Deconvolution.

http://dx.doi.org/10.1364/ao.XX.XXXXXX

1. INTRODUCTION

We previously described [1] a potentially significant and useful behavior of solutions of the time-dependent radiative transport equation (RTE) describing propagation of short pulses in a discrete-scatterer medium: if scatterers are large compared to the wavelength, the time-resolved intensity develops a sharply rising structure immediately following the coherent (ballistic) signal but attenuated at a significantly lower rate. This "early-time diffusion" (ETD) phenomenon can be understood in terms of the persistent random walk interpretation of the RTE: it is associated with those random-walk paths in which relative directions of the consecutive steps remain within the forward peak of the differential cross-section for scattering on an average medium constituent. In contrast, the ordinary "late-time diffusion" (LTD), responsible for the long tail of the observed signal, is associated with scattering at larger angles.

It follows, in particular, that the attenuation of the ETD signal is proportional not to the total cross-section (as for the coherent component), but only to the sum of the absorption cross-section (usually small in the optical range) and the cross-section for scattering at angles *outside* the narrow forward-scattering peak.

The original analysis identifying the ETD phenomenon [1] was done in the context of an omnidirectional source and the observed time-resolved intensity integrated over the energy flux angles, hence it did not directly involve angular flux distributions. Subsequently [2], we analyzed properties of the early-time diffusion signal for strongly collimated sources (narrow beams); such a scenario pertains to optical communication applications. We found that in this case the ratio of the ETD signal to the LTD contribution may be much (orders of magnitude) higher than for a wide beam. This fact can be explained in terms of the eigenmodes of the RTE: the modes contributing to

the early-time part of the signal have also narrow angular energy flux distributions and thus couple more strongly to a narrow than to a wide transmitted beam.

Here we extend the analysis to reflection-type imaging through an obscuring scattering medium, involving a two-way signal propagation – from the source to the observed object and back to the detector; the image is formed by isolating the ETD component of the propagating pulse. The main envisaged application is imaging through particulate obscuring atmospheric media, such as clouds, fog, mist, and aerosols.

Our main result is development a regularized-deconvolution technique which allows a *significant resolution improvement* by enhancing higher Fourier components of the PSF, based on the theoretically predicted point-spread function (PSF) associated with scattering in the medium.

The content of the paper is as follows:

Estimates of the angular and temporal spreads of pulses, based on the persistent random-walk model, are discussed in Section 2. Imaging scenarios, in which the image is formed by isolating the ETD component of the observed intensity are described in Section 3. Computation of the point-spread function (PSF) describing broadening of the angular energy flux distribution caused by scattering of the pulse in the medium constitutes an important element of our analysis (Section 4). High-accuracy solutions of the RTE enable us to reliably evaluate high Fourier components of the PSFs, including the incoherent ETD contributions and a transition to the region dominated by the coherent (ballistic) scattering. We find that the angular resolution of the directly formed ETD-based images is comparable to the width of the forward-scattering cross-section on the medium constituents. However, the directly formed images do not utilize the full range of Fourier components associated with the ETD signal (characterized by attenuation lower than for the coherent signal). Those components can be augmented by regularized deconvolution techniques (Section 5), leading to a significant resolution improvement, typically by the factor of 3 or 4 for propagation at the distance of about 20 mean free paths. Our main findings, including a simulation of the directly formed ETD-based image and its deblurred counterpart, are summarized in Section 6.

2. PROPERTIES OF THE ETD SIGNAL

The main features of the ETD phenomenon can be qualitatively explained by means of the persistent random walk on the sphere of flux directions (or, to a good approximation, on the plane of transverse directions). [1] We consider propagation of a beam, originally along the z axis, at the distance R; we denote the mean-free path [2] in the medium by ℓ_t and assume the differential scattering cross-section on an average medium constituent has a narrow forward-scattering peak of the width θ_0.

Then, with small-angle approximations, the transverse (or angular) distance traveled in n steps of the random walk will be

$$\theta_n \approx \sqrt{n}\,\theta_0\,. \tag{1}$$

Assuming a propagation distance R in the medium, there will be $N \sim R/\ell_t$ steps in the random walk, hence the total scattering angle will be

$$\Delta\theta \sim \sqrt{\frac{R}{\ell_t}}\,\theta_0\,. \tag{2}$$

At the same time, the z distance traveled in the n-th step is only

$$z_n = \ell_t \cos\theta_n \approx \ell_t\,(1-\tfrac{1}{2}\,\theta_n^2) \tag{3}$$

rather than ℓ_t. Therefore, the total defect in the distance traveled in the z direction (compared to the straight-line) is

$$\Delta z \approx \frac{\ell_t}{2}\sum_{n=1}^{N}\theta_n^2 \approx \frac{\ell_t\,\theta_0^2}{2}\sum_{n=1}^{N} n \approx \frac{\ell_t\,\theta_0^2\,N^2}{4} \sim \frac{R^2}{4\,\ell_t}\,\theta_0^2\,, \tag{4}$$

and the time delay is given by $\Delta t = \Delta z/v_0$, where $v_0 \approx c$ is the coherent-wave propagation speed in the medium. The width of the forward-scattering peak can be, further, estimated as $\theta_0 \sim 1/(k_0 a)$, where a is the scatterer radius and $k_0 = 2\pi/\lambda_0$ is the center wave number of the pulse. The estimates (2) and (4) are in a qualitative agreement with the parameters derived from actual RTE solutions, [3]

$$\Delta\theta_{\rm ETD}(R) \approx \kappa_\theta\sqrt{\frac{R}{\ell_t}}\,\frac{1}{k_0 a} \tag{5}$$

and

$$\Delta t_{\rm ETD}(R) \;\approx \kappa_\theta^2\,\frac{R^2}{v_0\,\ell_t}\,\frac{1}{(k_0 a)^2}\,, \tag{6}$$

with a numerical coefficient $\kappa_\theta \lesssim 0.3$ (see [1]).

In the calculations reported in this paper we assume parameters typical of optical propagation through an atmospheric cloud, fog, or mist: $\lambda_0 = 0.633\,\mu$m, $a = 5\,\mu$m $\approx 8\,\lambda_0$, hence $k_0\,a \approx 50$. The assumed number density of water droplets will be $n_0 = 10^9\,{\rm m}^{-3}$, resulting in a relatively short mean free path $\ell_t \approx 7\,$m.

With the above parameters, the estimated angular and temporal widths of the ETD signal for a distance $R = 16\,\ell_t$ are

$$\Delta\theta_{\rm ETD}(R) \approx 0.024\,{\rm rad}\,, \qquad \Delta t_{\rm ETD}(R) \approx 0.2\ {\rm ns}\,. \tag{7}$$

[1] Such a description is related to the Fokker-Planck approximation to the RTE, discussed already in [3] and followed by many later developments, e.g., [4–6].

[2] This quantity is given by $\ell_t = 1/(n_0\,\sigma_t)$, where n_0 is the medium number density and σ_t the ensemble-averaged total cross-section on a single medium constituent. Further details are given in Appendix A.

[3] The value of $\Delta\theta_{\rm ETD}(R)$ represents the width of the point-spread function and depends on the procedure of its extraction from the RTE computation (Section 4), hence it cannot be directly identified with the estimate (2) based on a simple model.

For comparison, the time scale of the ordinary, late-time diffusion (LTD) is $\ell_t/v_0 \approx 20\,\text{ns}$. Accordingly, we will consider transmitted pulses shorter than the ETD time scale, typically of duration $T_t \lesssim 0.1\,\text{ns}$, and in isolating the ETD signal (as described below), we will use filters of temporal width T_f somewhat larger than the ETD time scale and much smaller than the LTD time scale.

3. THE IMAGING SCENARIO

We concentrate here on a "photographic" (non-scanning) imaging scenario, where the scene is illuminated by a relatively wide (pulsed) beam and the image is taken by a camera – almost literally, except that each pixel in the camera sensor records intensity as a function of time. In an alternative, scanning, imaging scheme, a narrow pulsed beam moves across the scene, illuminates individual patches, and the reflected light is registered by a "single-pixel camera", i.e., an optical sensor which has no angular resolution. Because of reciprocity, the two imaging methods yield the same angular resolution; we consider here the first, which appears conceptually (if not technically) simpler.

For definiteness, we consider a flat scene covered by a layer of an obscuring medium (such as fog, smoke, or other aerosol) of thickness L. In the assumed active optical imaging scenario (Fig. 1) the pulsed beam source and the detector (the camera) is located at the height H directly above the objects(s) of interest.[4] A large area of the scene (much larger than the expected resolution) is illuminated by a divergent beam of angular width Θ (Fig. 1(a)) and the reflected light is observed by a camera collocated with the beam source (Fig. 1(b)). The pixels of the camera have the ability of recording the time dependence of the detected intensity, hence the camera provides measures a time- and angle-resolved light intensity.

It should be stressed that, although the above imaging scheme is described in the language of atmospheric remote sensing, a closely analogous procedure could be applied to, e.g., medical imaging through a layer of a biological tissue.

[4]The above assumptions are made for simplicity only; the treatment can be generalized to a medium layer located above the scene and to a slanted-view geometry. Although in that case evaluation of the PSF is more involved, the results remain, qualitatively, unchanged.

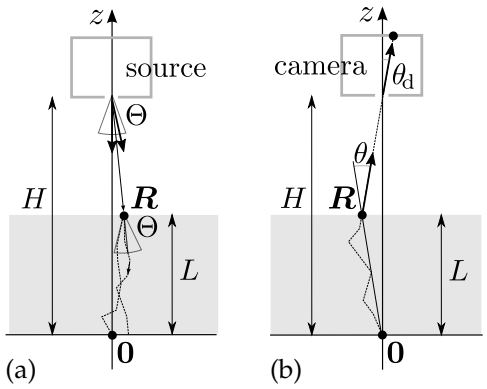

Fig. 1. A schematic representation of the considered imaging scenario. (a): A pulsed beam of width Θ illuminates the scene; the light enters the medium layer and, from each entry point $\boldsymbol{R}$, travels a distance $|\boldsymbol{R}| \approx L$, undergoing multiple scattering. (b): A camera located above the medium slab and looking at the scene detects light reflected from a diffusively scattering object located at $\boldsymbol{R} = \boldsymbol{0}$ on the scene; the reflected pulse again undergoes multiple scattering in the medium until it emerges from the medium at a point $\boldsymbol{R}$, $|\boldsymbol{R}| \approx L$. Deviations of the light propagation path from straight lines are greatly exaggerated (the actual angles are of the order of several hundredths of a radian).

In the above scenario the illuminating short pulse is assumed to have a certain time profile $A(t)$ and a certain angular width Θ. On its way to the scene, the beam passes through the layer and undergoes scattering, which causes its spread in time,[5] such that its evolved time dependence becomes $A_R(t)$.

In the optical domain, most objects of interest are diffuse scatterers; therefore, reflecting points on the scene can be considered secondary intensity sources, practically omnidirectional, emitting pulses of time profiles $A_R(t)$.

The reflected pulse due to a scatterer located at the origin (Fig. 1(a)) propagates through the medium layer and undergoes further scattering, until it emerges from the upper boundary of the layer and then travels along a straight line through the camera lens to form an image on the camera's focal plane. More precisely, each pulse is registered as a time-dependent intensity distribution at pixel locations uniquely related to the angles at which the light enters the camera aperture.

In the configuration of Fig. 1(b) and in the absence the medium, the light reflected from the object would travel to the detector along the z axis, i.e., the angle θ_d at which the light enters the camera aperture woudl always be zero. Scattering in the medium causes deviations from straight-line propagation, hence the light leaving the medium at some point $\boldsymbol{R}$ (Fig. 1(b)) may travel at an angle θ relative to the straight-line path. Since we will isolate the early-time component of the pulse, we may assume that the

[5] The scattering-induced angular spread is small compared to the assumed already wide beam, and practically does not affect scene illumination.

relevant angles are small (the estimates (2) and (5)). In this small-angle approximation, the scattering angle θ and the arrival angle $\theta_{\rm d}$ are related by

$$\theta_{\rm d} \approx \frac{L}{H}\,\theta\,. \tag{8}$$

The relation Eq. (8) means that the width of the distribution of the arrival angle $\theta_{\rm d}$ (which determines the image angular resolution) is proportional (with the coefficient $L/H \le 1$) to the width of the distribution of the angle θ at which the light is scatterered in the medium.

This fact allows us to simplify the geometry of the problem by placing the camera at the top of the medium layer (Fig. 2(b)) and characterizing the image resolution in terms of the distribution of the energy flux direction (a unit vector $\hat{\mathbf{s}}$ and the related angle θ) at the detection point $\boldsymbol{R}$.

By comparing Figs. 1(a) and 2(a) we can also simplify the the description of the bem propagation from the source to the scene: In Fig. 1(a) the pulse emitted by the source travels, before entering the medium, without changing its time dependence or tranverse flux distribution. Therefore, the source can be, as well, placed on top of the medium layer, as in 2(a), without changing the time dependence of the intensity illuminating the scene.

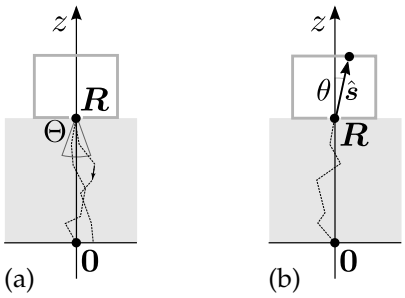

Fig. 2. A simplified imaging scenario with the source and detector located just above the medium layer.

To summarize, the angular resolution of the image seen by the camera in Fig. 1(b) can be obtained by considering the simplified scenario of Fig. 2, evaluating the point spread function (PSF) for that problem, and then reducing the angle spread by the factor L/H of Eq. Eq. (8).

4. COMPUTATION OF THE PSF

We describe here the procedure of using solutions of the RTE to evaluate the PSF expected to arise in the imaging scenario discussed in the previous Section, first on the conceptual (Subsections A and B) and then computational (Subsections C and D) levels.

A. The received radiance

As discussed in the previous Section, the radiance observed by the camera in the simplified imaging scenario can be described as resulting from two consecutive processes:

I: **Downward propagation** (Fig. 2(a)). The scene is illuminated by a source located at the point $\boldsymbol{R} = (0,0,R)$ on the upper boundary of the medium slab, emitting a pulsed beam of a certain initial intensity time profile $A(t)$ of width $T_{\rm p}$ and an angular distribution $B(\cos\theta)$ of some width $\Theta \ll 1$. For definiteness, we assume here Gaussians,

$$A(t) = \frac{\mathrm{e}^{-t^2/2T_{\rm p}^2}}{\sqrt{2\pi}\,T_{\rm p}}\,, \tag{9a}$$

$$B(\cos\theta) = \frac{\mathrm{e}^{-(1-\cos\theta)/\Theta^2}}{2\pi\,\Theta^2} \approx \frac{\mathrm{e}^{-\theta^2/2\Theta^2}}{2\pi\,\Theta^2}\,, \tag{9b}$$

normalized to $\int_{-\infty}^{\infty}\mathrm{d}t\,A(t) = 1$, $\int_{-1}^{1}\mathrm{d}\cos\theta\,B(\cos\theta) \approx 1$. As a result of propagation to the reflecting point on the scene, the pulse time-dependence becomes a stretched profile $A_R(t)$, dependent on the propagation distance R and the initial beam width Θ.

Since we are only concerned with the ETD signal, we can replace the medium slab with an infinite medium, since any propagation paths extending outside the interval $0 \le z \le L$ will be too long to contribute to the observed intensity within the ETD time range.

Now, the intensity profile $A_R(t)$ arising in the process I is the convolution of the Green function Γ with the initial pulse temporal and angular distributions, integrated over the final flux directions (since the object is assumed to reflect light independently of the incidence angle). Therefore,

$$A_R(t) = \int \mathrm{d}t' \int \mathrm{d}\cos\theta\; I(t-t', R, \cos\theta)\, A(t')\, B(\cos\theta)\,, \tag{10}$$

with the radiance

$$I(t, R, \cos\theta) \equiv I(t, |\boldsymbol{R}|, \hat{\boldsymbol{R}}\cdot\hat{\mathbf{s}}) = \int \mathrm{d}^2\hat{s}'\,\Gamma(t, \boldsymbol{R}; \hat{\mathbf{s}}, \hat{\mathbf{s}}')\,, \tag{11}$$

given by the Green function of the RTE (Appendix A) integrated over the final energy flux direction, hence a function of only the propagation time and distance, as well as the cosine of the angle θ between the propagation and the initial flux direction.

II: **Upward propagation** (Fig. 2(b)). The point object on the scene reflects, diffusively (omnidirectionally), the pulse $A_R(t)$ and the evolved pulse is detected by the camera collocated with the source. The camera is assumed to register the light intensity as function of time t and of the arrival angle θ.

As a result of the process II, the received radiance, say I_A, is the convolution of the time profile of the reflected pulse and the same as before radiance (11),

$$I_A(t, R, \cos\theta) = \int \mathrm{d}t'\, I(t-t', R, \cos\theta)\, A_R(t')\,, \tag{12}$$

where now θ is the angle between the propagation and the received energy flux directions (Fig. 2(b)).

B. Image formation and the PSF

The image of the considered point object, represented by the radiance Eq. (12), can be now identified with the point-spread function which, in turn, will provide an estimatede of the image resolution.

The radiance (12) contains both the early- and the late-time diffusion contributions, the latter having a very wide angular flux distribution and thus of no use in imaging. In order to isolate the first, ETD, component, we apply to $I_A(t,R,\cos\theta)$ an appropriate high-pass filter Φ and obtain [1, 2] the convolution

$$I_{\Phi,A}(t,R,\cos\theta) \equiv \big(\Phi(\cdot)\circ I_A(\cdot,R,\cos\theta)\big)(t) := \int \mathrm{d}t'\,\Phi(t-t')\,I_A(t',R,\cos\theta)\,; \quad \textbf{(13)}$$

the latter quantity, still time-dependent, will be significant only in a short interval containing the ETD signal.

The actual image will be formed based on intensities measured by pixels on the focal plane located at points $\boldsymbol{q}$ relative to the optical axis of the camera. With no loss of generality we can express the distances $q=|\boldsymbol{q}|$ in units of the focal length, which implies that the arriving energy flux direction can be approximated (for small angles) by $\hat{\boldsymbol{s}}=(\boldsymbol{q},1-q^2/2)$ or, equivalently, by setting $\cos\theta=1-q^2/2$, $0\le q\le 2$.

The filtered intensity Eq. (13) – still time-dependent – is not, in general, positive definite. Therefore, we propose that the actual "intensity image" (in the present case, the point-spread function) is formed defined by taking the absolute value of the filtered intensity (13) and integrating it over a time interval containing its peak. The postulated expression for the PSF is thus

$$\Lambda(R;q)=\int_{t_1}^{t_2}\mathrm{d}t\,\big|I_{\Phi,A}\big(t,R,1-\tfrac{1}{2}\,q^2\big)\big| \quad \textbf{(14)}$$

where the integration limits t_1 and t_2 can be automatically determined on the basis of the shape of the filtered signal, without any a-priori knowledge of the arrival time of the pulse.

For an arbitrary scene, our prescription for image formation is

$$F(R;\boldsymbol{q})=\int_{t_1}^{t_2}\mathrm{d}t\,\big|\Phi(\cdot)\circ I\big(\cdot,R,\boldsymbol{q},1-\tfrac{1}{2}\,q^2\big)\big|\,, \quad \textbf{(15)}$$

where $I(t,R,\hat{\boldsymbol{s}})$ is the radiance measured by the camera.

C. Implementation

The PSF (14) is defined in terms of the received radiance (12) and, ultimately, in terms of the basic radiance (11). The latter quantity, as discussed in Appendix A, is given as the partial-wave expansion (46) with the coefficients (47) computed directly from the solution of the RTE.

Our experience has shown that one should avoid directly storing and operating on rapidly varying functions of θ, such as the radiances and the resulting PSF, tabulated at uniformly distributed θ points. It is more economical to use Gauss-Legendre quadrature points or, alternatively, store the function in its partial-wave (l) representations. Therefore, we operate as much as possible in the "l-space" and only at the end of the computation synthesize the appropriate Fourier-Legendre series, such as (46) and, eventually, construct the PSF (14).

Computation of the radiances. The first stage of the computation is to obtain the solution of the time-dependent RTE, as described in Appendix A. The time- and angle-resolved radiance (11) is represented by Eq. (46) in terms of its partial-wave components I_l which, in turn, are given by Eq. (47), in terms of the eigenvalues and eigenfunctions of the RTE operator; their properties – especially those pertaining to the early-time behavior of the solution – are also discussed in the Appendix.

Next, the partial-wave radiance components $I_l(t,R)$ are used to evaluate the quantities (10) and (12) associated with downward (I) and upward (II) propagation are expressed in terms of the RTE solutions:

I: With the angular source distribution (9b) and the expansion (46), the evolved pulse profile $A_R(t)$ is given by

$$\begin{aligned} A_R(t) &= \sum_{l=0}^{\infty}\int \mathrm{d}t'\,I_l(t-t',R)\,A(t')\int \mathrm{d}\cos\theta\,\mathrm{P}_l(\cos\theta)\,B(\cos\theta) \\ &= \sum_{l=0}^{\infty} C_l(\Theta)\int \mathrm{d}t'\,I_l(t-t',R)\,A(t') \end{aligned} \quad \textbf{(16)}$$

with the coefficients ([7], Eq. (2.17.5.2))

$$C_l(\Theta)=\frac{2}{\Theta^2}\,\mathrm{e}^{-1/\Theta^2}\,\mathrm{i}_l\!\left(\frac{1}{\Theta^2}\right) \quad \textbf{(17)}$$

$$\overset{\Theta\ll l}{\sim} 1-\frac{l\,(l+1)}{2}\,\Theta^2+\frac{l\,(l+1)\,[2\,l\,(l+1)+1]}{16}\,\Theta^4+\cdots$$

given in terms of modified spherical Bessel functions $\mathrm{i}_l(x)\equiv \mathrm{i}_l^{(1)}(x)$ ([8], Eq. (10.47.7)). [6] In practice, for $\Theta\ll 1$, $C_l(\Theta)$ is very well approximated by $\exp(-\Theta^2\,l^2/2)$ [2].

II: The radiance distribution (12) observed by the detector can be also represented, as in Eq. (46), in terms of its partial-wave projections, given by

$$I_{A,l}(t,R)=\int \mathrm{d}t'\,I_l(t-t',R)\,A_R(t')\,. \quad \textbf{(18)}$$

Computation of the PSF. Further, high-pass time filtering (Eq. (13)) isolates the ETD components of the received partial-wave intensities,

$$I_{\Phi,A,l}(t,R)=\int \mathrm{d}t'\,\Phi(t-t')\,I_{A\,l}(t',R)\,, \quad \textbf{(19)}$$

Finally, the last partial-wave representation is converted to the filtered radiance (13),

$$I_{\Phi,A}(t,R,1-q^2/2) = \sum_{l=0}^{\infty}\sqrt{2l+1}\;\mathrm{P}_l\big(1-\tfrac{1}{2}\,q^2\big)\,I_{\Phi,A,l}(t,R)\,, \quad \textbf{(20)}$$

[6] The last expansion in Eq. (17) is useful, because typical implementations (such as the `gsl` package) may fail in the region of moderate l ($\lesssim 150$) and small Θ ($\lesssim 10^{-3}$).

which is integrated to obtain the PSF (14), as a function of the image coordinates $q = |\boldsymbol{q}|$.

In view of the deblurring procedure, to be discussed in Sec. 5, we also evaluate the two dimensional Fourier transform (Hankel transform) of the PSF, as a function of the spatial frequency $\varrho = |\boldsymbol{\varrho}|$,

$$\widetilde{\Lambda}(R,\varrho) = \int \mathrm{d}^2 q\, \mathrm{e}^{-\mathrm{i}\,\boldsymbol{\varrho}\cdot\boldsymbol{q}}\, \Lambda(R,\boldsymbol{q}) = 2\pi \int_0^2 \mathrm{d}q\, q\, \mathrm{J}_0(\varrho\, q)\, \Lambda(R,\boldsymbol{q})\,. \qquad (21)$$

In particular, the above quantity, normalized to unity at zero frequency,

$$\widetilde{M}(R,\varrho) = \frac{\widetilde{\Lambda}(R,\varrho)}{\widetilde{\Lambda}(R,0)}\,, \qquad (22)$$

is the conventional modulation transfer function (MTF).

D. Results for the PSF

The following describes the actual computational procedure, with the order of operations (sums, integrals, filtering, etc.) designed to optimize its efficiency.

The RTE theory predicts that the temporal width of the ETD signal should be proportional to the propagation distances squared; hence, with increasing the distance from $R/\ell_\mathrm{t} = 16$ to $R/\ell_\mathrm{t} = 24$, the filter width T_f should increase by the factor $(24/16)^2 = 2.25$. Correspondingly, for $R/\ell_\mathrm{t} = 16$ we use a filter of width $T_\mathrm{f} = 0.010\,\ell_\mathrm{t}/v_0$ and for $R/\ell_\mathrm{t} = 16$ a filter of width $T_\mathrm{f} = 0.020\,\ell_\mathrm{t}/v_0$.

Computations of the PSF have been carried out for a high angular-momentum truncation $l < N$, $N = 1600$, using the procedure discussed above, and the RTE solutions obtained as described in Appendix A. Dependence of the solutions on the truncation and the character of its convergence for $N \to \infty$ is further discussed in Ref. [2]. The results obtained for the MFT (22) are plotted in Fig. 3. The MFT provides, essentially, the same information as contained in its Fourier transform, the PSF; in particular, the inverse of the width of the MTF determines the angular resolution of the PSF (‚easured in radians).

For comparison, we also plot in this Figure the Hankel transform of the ensemble-averaged differential scattering cross-section $\sigma(\cos\theta)$ on a medium consitituent,

$$\widetilde{\sigma}(\varrho) := 2\pi \int_0^2 \mathrm{d}q\, q\, \mathrm{J}_0(\varrho\, q)\, \sigma\big(1 - \tfrac{1}{2}\, q^2\big)\,. \qquad (23)$$

The presence of relatively high-ϱ components in the transform $\widetilde{\sigma}(\varrho)$ is indicative of a sharp forward-scattering ($\theta \approx 0$) peak in the cross-section. However, $\widetilde{\sigma}(\varrho)$ decays faster than exponentially and becomes negligibly small for $\varrho \gtrsim 200$. In contrast, the plotted MTF, after an initial exponential decay, flattens out, and remains nearly constant up to the maximum ϱ value, which is the truncation value $N = 1600$. The presence of such large Fourier components in the PSF suggests a potential possibility of recovering those components by means of regularized deconvolution and thus achieving a substantial improvement in the image angular resolution.

Fig. 4 shows the unnormalized Fourier transform $\widetilde{\Lambda}(R;\varrho)$ of the PSFs for the two considered propagation distances. It is evident that, with the increasing distance, the distribution at relatively small ϱ ($\varrho \lesssim 200$) decays at a lower rate than the large-ϱ components. This behavior indicates that the lower ϱ contributions are due to the early-time diffusion, while the highest ϱ components of the PSF can be, essentially, attributed to coherent (ballistic) propagation.

In the smaller ϱ range the ratio of the MTFs is

$$\frac{\widetilde{\Lambda}(24\,\ell_\mathrm{t};\varrho)}{\widetilde{\Lambda}(16\,\ell_\mathrm{t};\varrho)} \approx \mathrm{e}^{-0.64\cdot(24-16)}\,, \qquad (24)$$

in agreement with the prediction that the attenuation of the ETD signal should be about 65 % of the coherent signal attenuation [1]. At the same time, the large-ϱ ($\varrho \gtrsim 400\,\mathrm{rad}^{-1}$) part of the MTF decays at nearly the same rate as coherent scattering, the ratio in Fig. 4 being close to $\mathrm{e}^{-(24-16)} \approx 3.4\cdot 10^{-4}$; accordingly, we refer to these contributions as "quasi-coherent".

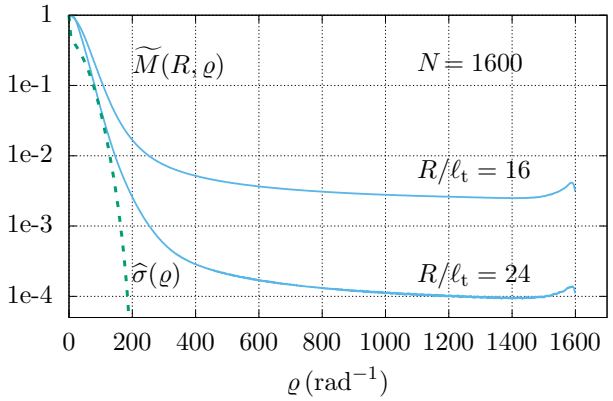

Fig. 3. Normalized MTFs computed with R-dependent high-pass filter widths.

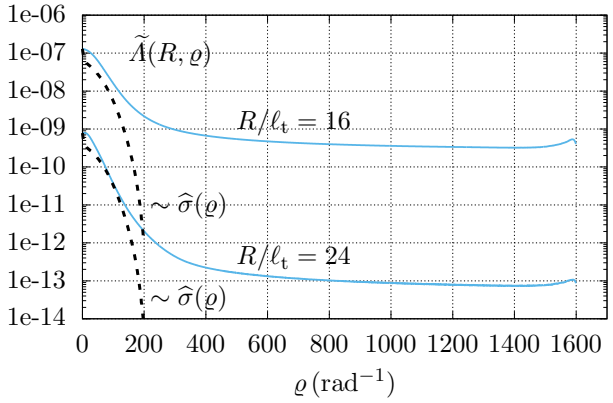

Fig. 4. Unnormalized MTFs computed with R-dependent high-pass filter widths.

5. DEBLURRING BY REGULARIZED DECONVOLUTION

A widely used approach to improving resolution of images is based on deconvolution with Tikhonov-type regularization (e.g., [9, 10]).

In the considered imaging scenario, linearity of the measured image intensity in the objects' reflectivity implies that the observed image is given by the convolution

$$F(\boldsymbol{q}) = (\Lambda \circ f)(\boldsymbol{q}) + \eta(\boldsymbol{q})\,, \tag{25}$$

where f is the ideal image (object) function, Λ is the PSF, and η a random function representing an additive noise. In Fourier space[7] convolutions become products,[8] hence recovering the unknown ideal image amounts to solving the (usually ill-posed) inverse problem

$$\widetilde{\Lambda}(\boldsymbol{\varrho})\,\widetilde{f}(\eta;\boldsymbol{\varrho}) = \widetilde{F}(\boldsymbol{\varrho}) - \widetilde{\eta}(\boldsymbol{\varrho}) \tag{26}$$

with its "exact" r.h.s. $\widetilde{F}$ perturbed by the noise, hence the dependence of the solution f on η.

A naive inverse filtering procedure amounts to constructing

$$\widetilde{f}(\eta;\boldsymbol{\varrho}) = \frac{\widetilde{F}(\boldsymbol{\varrho}) - \widetilde{\eta}(\boldsymbol{\varrho})}{\widetilde{\Lambda}(\boldsymbol{\varrho})}\,; \tag{27}$$

division by the Fourier-space PSF enhances large Fourier components of the observed image and improves the resolution. In particular, when applied to the PSF itself ($\widetilde{F} = \widetilde{\Lambda}$), inverse filtering would yield a constant in the Fourier space (hence a delta function in $\boldsymbol{\varrho}$), *provided* the noise contribution could be neglected.

However, the prescription Eq. (27) is well known to fail in many (if not most) realistic problems just because of the noise: while, typically, both $\widetilde{F}$ and $\widetilde{\Lambda}$ represent functions smoothly varying from pixel to pixel, and thus rapidly decaying for large $|\boldsymbol{\varrho}|$, the noise at different pixels is largely uncorrelated and thus its spectrum is very wide. For this reason, the noise contribution in Eq. (27) may, for large $|\boldsymbol{\varrho}|$, overwhelm the measured image data $\widetilde{F}(\boldsymbol{\varrho})$ – which is a symptom of the problem being ill-posed. Decades of research and experience in such problems suggest that in many situations an adequate solution solution is a simple regularized deconvolution

$$\widetilde{f}_\beta(\eta;\boldsymbol{\varrho}) = \frac{\widetilde{\Lambda}(\boldsymbol{\varrho})\,\big[\widetilde{F}(\boldsymbol{\varrho}) - \widetilde{\eta}(\boldsymbol{\varrho})\big]}{\widetilde{\Lambda}^2(\boldsymbol{\varrho}) + \beta^2} \tag{28}$$

with a real regularization parameter $\beta > 0$. The solution $\widetilde{f}_\beta(\eta;\boldsymbol{\varrho})$ is a result of minimizing a modified penalty function $|\widetilde{\Lambda}\widetilde{f} - (\widetilde{F} - \widetilde{\eta})|^2 + \beta^2\,|\widetilde{f}|^2$, instead of the original function $|\widetilde{\Lambda}\widetilde{f} - (\widetilde{f} - \widetilde{\eta})|^2$.

[7] In a practical implementation $\boldsymbol{q}$ would be discrete and would represent image pixels, hence the Fourier transform would be also a discrete one. In our problem $\widetilde{f}$, $\widetilde{F}$, and $\widetilde{\Lambda}$ are real.

[8] More generally, the discretized equation (26) can be diagonalized by applying to it the singular-value decomposition.

As it is known in general and will be seen in the procedure described below, the parameter β can be adjusted so that, depending on $\boldsymbol{\varrho}$, the noise contribution to $\widetilde{f}_\beta(\eta;\boldsymbol{\varrho})$ is much smaller than the signal (F) contribution, or both η and F contributions are negligibly small.

To assess the resolution improvement achievable with the described regularized deconvolution, we apply it to the PSF itself and define the "deblurred PSF" by

$$\widetilde{\Lambda}_\beta(\eta;\boldsymbol{\varrho}) = \frac{\widetilde{\Lambda}(\boldsymbol{\varrho})\,\big[\widetilde{\Lambda}(\boldsymbol{\varrho}) - \widetilde{\eta}(\boldsymbol{\varrho})\big]}{\widetilde{\Lambda}^2(\boldsymbol{\varrho}) + \beta^2}\,. \tag{29}$$

It is convenient to express the above deconvolution in terms of the (now time-independent) MTF defined by $\widetilde{M}_\mathrm{t}(\boldsymbol{\varrho}) = \widetilde{\Lambda}(\boldsymbol{\varrho})/\widetilde{\Lambda}(0)$ and the dimensionless noise $\hat{\eta}$ and regularization parameter $\hat{\beta}$, defined by

$$\hat{\eta}(\boldsymbol{\varrho}) := \frac{\widetilde{\eta}(\boldsymbol{\varrho})}{\widetilde{\Lambda}(\boldsymbol{0})}\,, \qquad \hat{\beta} := \frac{\beta}{\widetilde{\Lambda}(\boldsymbol{0})}\,. \tag{30}$$

We also assume here an approximately white noise, i.e., $\hat{\eta}(\boldsymbol{\varrho}) \approx$ const throughout the entire $\boldsymbol{\varrho}$ range (in the sense of the values of the autocorrelation of $\hat{\eta}$). In order to In the deblurred MFT,

$$\widetilde{M}_\beta(\eta;\boldsymbol{\varrho}) = \frac{\widetilde{M}(\boldsymbol{\varrho})\,\big[\widetilde{M}(\boldsymbol{\varrho}) - \hat{\eta}(\boldsymbol{\varrho})\big]}{\widetilde{M}^2(\boldsymbol{\varrho}) + \hat{\beta}^2}\,, \tag{31}$$

we have to take $\hat{\beta}$ satisfying the conditions

$$|\hat{\eta}(\boldsymbol{\varrho})| \ll \hat{\beta} \ll 1\,. \tag{32}$$

In analyzing the behavior of MFT Eq. (31), we can distinguish three regions:

(A) $\hat{\beta} \ll |\widetilde{M}(\boldsymbol{\varrho})| \le 1$: Here we have

$$\widetilde{M}_\beta(\eta;\boldsymbol{\varrho}) \approx \frac{\widetilde{M}(\boldsymbol{\varrho}) - \hat{\eta}(\boldsymbol{\varrho})}{\widetilde{M}(\boldsymbol{\varrho})}\,, \tag{33}$$

hence the signal contribution is nearly unity and the noise relative to the signal is small, $|\hat{\eta}(\boldsymbol{\varrho})|/|\widetilde{M}(\boldsymbol{\varrho})| \ll \hat{\beta} \ll 1$.

(B) $|\hat{\eta}(\boldsymbol{\varrho})| \ll |\widetilde{M}(\boldsymbol{\varrho})| \ll \hat{\beta}$: In this domain

$$\widetilde{M}_\beta(\eta;\boldsymbol{\varrho}) \approx \frac{\widetilde{M}(\boldsymbol{\varrho})\,\big[\widetilde{M}(\boldsymbol{\varrho}) - \hat{\eta}(\boldsymbol{\varrho})\big]}{\hat{\beta}^2} \tag{34}$$

and the signal contribution to $\widetilde{M}_\beta(\eta;\boldsymbol{\varrho})$ is small, $S(\boldsymbol{\varrho}) := \widetilde{M}^2(\boldsymbol{\varrho})/\hat{\beta}^2 \ll 1$. However, the noise component $N(\boldsymbol{\varrho})$ is even smaller, ensuring a small ratio $N(\boldsymbol{\varrho})/S(\boldsymbol{\varrho}) \approx |\hat{\eta}(\boldsymbol{\varrho})|/|\widetilde{M}(\boldsymbol{\varrho})| \ll 1$.

(C) $|\widetilde{M}(\boldsymbol{\varrho})| \ll |\hat{\eta}(\boldsymbol{\varrho})| \ll \hat{\beta}$: Here the approximation (34) still applies and yields extremely small signal *and* the noise, $S(\boldsymbol{\varrho}) \approx \widetilde{M}^2(\boldsymbol{\varrho})/\hat{\beta}^2 \lll 1$ and $N(\boldsymbol{\varrho}) \approx \widetilde{M}(\boldsymbol{\varrho})\,\widetilde{\eta}(\boldsymbol{\varrho})/\hat{\beta}^2 < \widetilde{\eta}^2(\boldsymbol{\varrho})/\hat{\beta}^2 \lll 1$.

As a reliable model of noise would have to depend on the details of the technical implementation of the considered imaging scheme, we rather assume a certain noise level, say η_0, and take $\hat{\beta}$ sufficiently large (Eq. (32)) to make the deconvolution result simply immune to noise.

The original MTF and the deconvolution result $\widetilde{M}_\beta(\eta;\boldsymbol{\varrho})$ are plotted in Figs. 5(a) and (b) for the two considered propagation distances. In both cases we assumed the noise η_0 at the level of the quasi-coherent large-$\boldsymbol{\varrho}$ contribution to the MTF, which means that the coherent component of the image is, in practice, unobservable. Correspondingly, we took $\hat{\beta} = 0.01$ and $\hat{\beta} = 0.001$, about 10 times higher than the noise level. In this sense, our deblurred PSF is dominated by the *incoherent* early-time-diffusion component of the signal. It is seen that the values of the deblurred MFT stay close to 1 in a considerable range of q values, hence a significant resolution improvement can be expected.

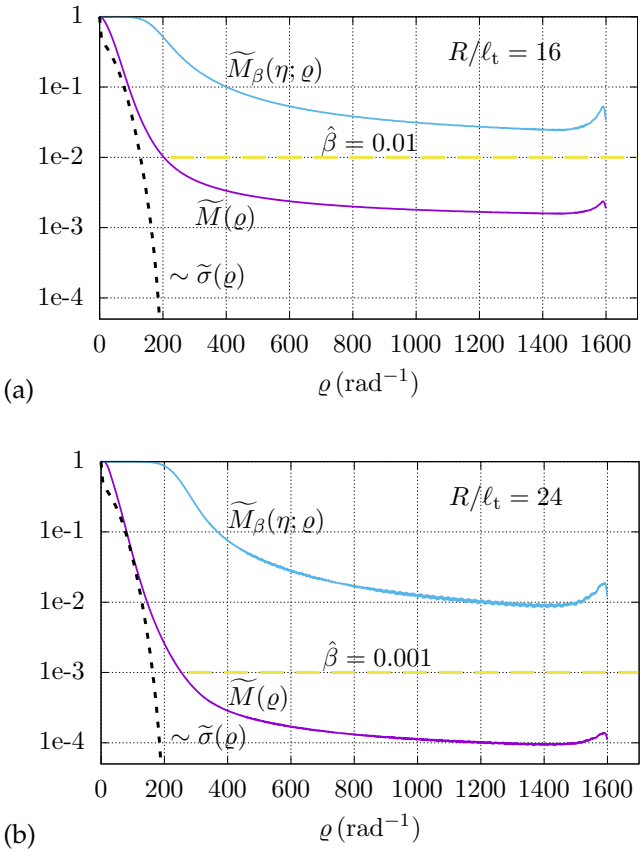

Fig. 5. MTFs for two layer thicknesses, original and after deconvolution, with the indicated values of the regularization parameter $\hat{\beta}$, under the assumption that the noise levels coincide with the levels of the high-ϱ tails of the original MFT. The shape of the Fourier transform of the scattering cross-section is plotted for comparison.

This expectation is confirmed in Figs. 6(a) and (b) which show the original PSF $\Lambda(\boldsymbol{\varrho})$ and the "deblurred PSF", i.e., the absolute value of the inverse Fourier transform $M_\beta(\eta;q) \equiv \Lambda_\beta(\eta;q)/\Lambda_\beta(\eta;0)$ of the function $\widetilde{M}_\beta(\eta;\varrho)$, both normalized to their values at $q = 0$. It is evident that the distribution of M_β is significantly narrower than that of Λ and the differential cross-section σ. The above statement holds not only for the smaller propagation distance (for which there is still a significant coherent component contribution, represented by the narrow component of Λ) but also for $R/\ell_t = 24$, for which the coherent component is negligible.

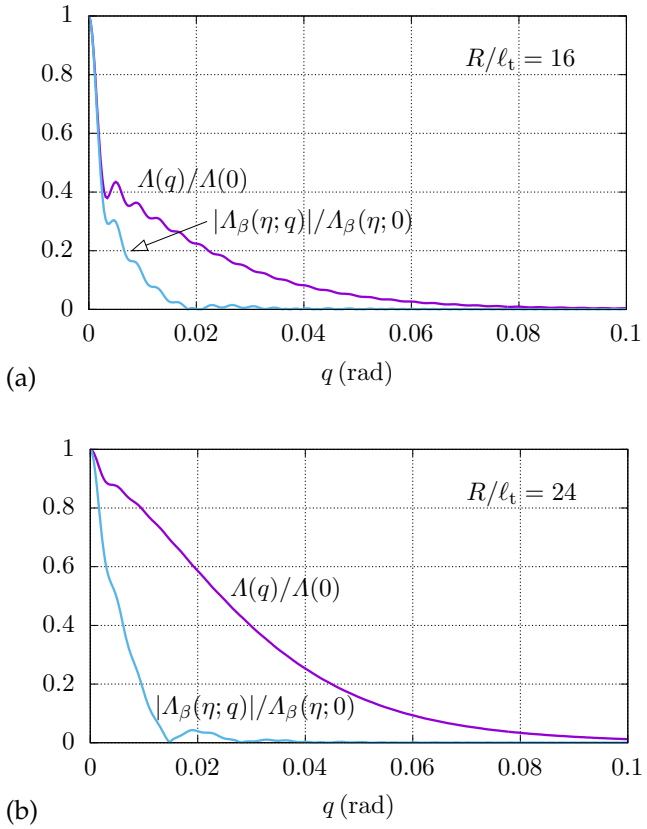

Fig. 6. Original and deblurred PSFs for two layer thicknesses, $R/\ell_t = 16$ and $R/\ell_t = 24$. The FWHM widths of the distributions are, approximately, 0.004 and 0.010 radians.

Finally, Fig. 7 shows a simulated image (for $R/\ell_t = 24$) of two point objects separated by the angle of 0.015 radians, corresponding to the original (a) and deblurred (b) PSFs. After deblurring, the two points are clearly distinguishable, although still surrounded by halos, which will, generally, reduce the image contrast.

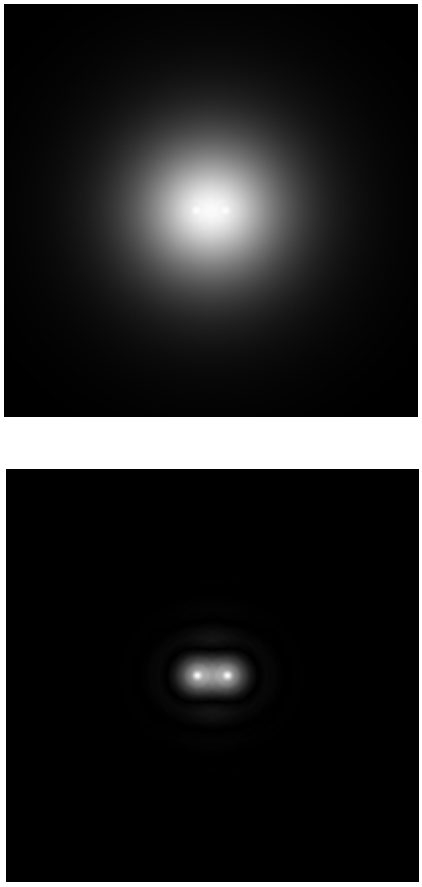

Fig. 7. Simulated images, before (a) and after (b) deblurring, for $R/\ell_{\rm t} = 24$ and for the angular distance of 0.015 radians between the two point objects.

6. SUMMARY

In this paper we extended the previous treatment of the early-time diffusion (ETD) phenomenon to the description of an imaging scenario involving a two-way propagation of a short pulse through a layer of a random medium. We carried out a detailed analysis of the angular distributions of the energy flux in solutions of the time-dependent RTE, resulting in computation of the point-spread function (PSF) based on the extracted ETD component of the image.

The obtained PSF and the corresponding modulation transfer function (MTF) characterizes both the incoherent ETD contribution (i.e., lower Fourier components of the PSF) and the quasi-coherent ETD contribution (the highest Fourier components), as well as the important transition between the two regions. The computation, which included very high angular momenta ($l > 1000$), was facilitated by development of a novel analytic technique allowing efficient transformation between angular momenta in the RTE solution and the Fourier components of the PSF.

The angular resolution implied by the computed PSF is controlled by the behavior of the dominant RTE modes responsible for the ETD signal and is comparable to the angular width of the scattering cross-section. We then showed that, by using regularized deconvolution techniques, one can significantly improve the angular image resolution by effectively enhancing higher Fourier components ϱ of the PSF, up to the highest ϱ values for which the radiance is still attenuated at a reduced rate. This finding, illustrated in Sec. 5, may further improve the prospects of application of the ETD phenomenon in imaging.

ACKNOWLEDGMENT

This material is based upon work supported by the U. S. Air Force Office of Scientific Research under award number FA 9550-16-C-0014.

A. SUMMARY OF THE RTE AND A SOLUTION TECHNIQUE

The RTE [3, 11–13] for the coordinate space Green function Γ in an unbounded statistically homogeneous random medium can be written in the standard form

$$\left(\mu_{\rm t} + v_0^{-1}\,\partial_t + \hat{\boldsymbol{s}}\cdot\boldsymbol{\nabla}_{\boldsymbol{R}}\right)\Gamma(t,\boldsymbol{R};\hat{\boldsymbol{s}},\hat{\boldsymbol{s}}') \qquad (35)$$
$$-\int \mathrm{d}^2\hat{\boldsymbol{s}}''\,\Sigma(\hat{\boldsymbol{s}}\cdot\hat{\boldsymbol{s}}'')\;\Gamma(t,\boldsymbol{R};\hat{\boldsymbol{s}}'',\hat{\boldsymbol{s}}') = \delta(t)\,\delta^3(\boldsymbol{R})\,\delta^2(\hat{\boldsymbol{s}}-\hat{\boldsymbol{s}}')\,;$$

here $\Gamma(t,\boldsymbol{R};\hat{\boldsymbol{s}},\hat{\boldsymbol{s}}')$ is the radiance at the observation point $(t,\boldsymbol{R})$ due an infinitely short pulse emitted at the time $t = 0$ from the origin $\boldsymbol{R} = \boldsymbol{0}$ in the direction $\hat{\boldsymbol{s}}'$ ($|\hat{\boldsymbol{s}}| = |\hat{\boldsymbol{s}}'| = 1$). The differential operator in the first line of the RTE (35) represents pulse propagation along a straight line, with the velocity $v_0 \approx c$ (for a dilute medium) and with the attenuation coefficient (the inverse of the maen free path) $\mu_{\rm t} = 1/\ell_{\rm t} = n_0\,\sigma_{\rm t}$, where n_0 is the number density of the medium and $\sigma_{\rm t}$ is the ensemble-averaged total cross section on a single scatterer. Scattering in the medium is described by the kernel $\Sigma(\hat{\boldsymbol{s}}\cdot\hat{\boldsymbol{s}}') = n_0\,\sigma(\hat{\boldsymbol{s}}\cdot\hat{\boldsymbol{s}}')$, proportional to the (also ensemble-averaged) differential scattering cross-section σ on a single medium constituent.

After decomposing the Green function in plane waves of frequencies Ω and wave vectors $\boldsymbol{P}$,

$$\Gamma(t,\boldsymbol{R};\hat{\boldsymbol{s}}'',\hat{\boldsymbol{s}}') = \int\frac{\mathrm{d}\Omega}{2\pi}\int\frac{\mathrm{d}^3P}{(2\pi)^3}\;\mathrm{e}^{-\mathrm{i}\,\Omega\,t}\,\mathrm{e}^{\mathrm{i}\,\boldsymbol{P}\cdot\boldsymbol{R}}\;\widetilde{\Gamma}(\Omega,P;\hat{\boldsymbol{s}},\hat{\boldsymbol{s}}')\,, \qquad (36)$$

the integro-differential equation (35) becomes

$$\left(\mu_{\rm t} - \mathrm{i}\,v_0^{-1}\,\Omega + \mathrm{i}\,P\,\hat{\boldsymbol{z}}\cdot\hat{\boldsymbol{s}}\right)\widetilde{\Gamma}(\Omega,P;\hat{\boldsymbol{s}},\hat{\boldsymbol{s}}') \qquad (37)$$
$$-\int \mathrm{d}^2\hat{\boldsymbol{s}}''\,\Sigma(\hat{\boldsymbol{s}}\cdot\hat{\boldsymbol{s}}'')\;\widetilde{\Gamma}(\Omega,P;\hat{\boldsymbol{s}}'',\hat{\boldsymbol{s}}') = \delta^2(\hat{\boldsymbol{s}}-\hat{\boldsymbol{s}}')\,.$$

Here the wave vector $\boldsymbol{P}$ has been taken along the z axis, since a general solution can be obtained from this one by a simple rotation.

In the angular-momentum formulation, the Green function in the RTE (37) is expanded in spherical harmonics,

$$\widetilde{\Gamma}(\Omega,P;\hat{\boldsymbol{s}},\hat{\boldsymbol{s}}') = \sum_{m,l,l'} \mathrm{Y}_{l,m}(\hat{\boldsymbol{s}})\,\mathrm{Y}^*_{l',m}(\hat{\boldsymbol{s}}')\,\Gamma^m_{l,l'}(\Omega,P)\,. \qquad (38)$$

By substituting the above expansion in Eq. (37) and projecting the equation on the same set of spherical harmonics, one obtains an infinite system of equations

$$\sum_{l''} M^m_{l,l''}(\Omega,P)\,\Gamma^m_{l'',l'}(\Omega,P) - \Sigma_l\,\Gamma^m_{l,l'}(\Omega,P) = \delta_{l,l'}\,, \quad \textbf{(39)}$$

where

$$\Sigma_l = 2\pi\int_{-1}^{1} \mathrm{d}x\,\mathrm{P}_l(x)\,\Sigma(x) \quad \textbf{(40)}$$

and

$$\begin{aligned} M^m_{l,l'}(\Omega,P) &= (\mu_\mathrm{t} - \mathrm{i}\,v_0^{-1}\,\Omega)\,\delta_{l,l'} + \mathrm{i}\,P\,B^m_{l,l'} \\ &\equiv -\,\mathrm{i}\,v_0^{-1}\,\Omega\,\delta_{l,l'} + M^m_{l,l'}(P)\,, \end{aligned} \quad \textbf{(41)}$$

with

$$\begin{aligned} B^m_{l,l'} &= \int \mathrm{d}^2\hat{s}\;\mathrm{Y}^*_{l,m}(\hat{s})\,\hat{z}\cdot\hat{s}\;\mathrm{Y}_{l',m}(\hat{s}) \\ &= \delta_{l,l'+1}\,b^m_l + \delta_{l',l+1}\,b^m_{l'}\,, \end{aligned} \quad \textbf{(42)}$$

where $b^m_l = \sqrt{(l^2-m^2)/(4l^2-1)}$.

The Green function, truncated to N partial waves ($l < N$), can be then represented as

$$\Gamma^m_{l,l'}(\Omega,P) = \mathrm{i}\,v_0\sum_{j=1}^{N}\frac{w^m_{j,l}(P)\;w^m_{j,l'}(P)}{\Omega-\Omega^m_j(P)} \quad \textbf{(43)}$$

in terms of frequency eigenvalues $\Omega^m_j(P)$ and eigenvectors $w^m_j(P)$ of the equation

$$M^m(P)\,w^m_j(P) = \mathrm{i}\;v_0^{-1}\,\Omega^m_j(P)\;w^m_j(P)\,. \quad \textbf{(44)}$$

As can be seen, e.g., from Eqs. (36), (46), and (47), the imaginary parts of the frequency eigenvalues control attenuation coefficients μ of the radiance modes and their real parts yield the modes' propagation velocities v,

$$\mu^m_j(P) = -\,\frac{\mathrm{Im}\,\Omega^m_j(P)}{v_0}\,, \qquad v^m_j(P) = \frac{\mathrm{Re}\,\Omega^m_j(P)}{P}\,. \quad \textbf{(45)}$$

As discussed in [2], the eigenvalues $\Omega^m_j(P)$ can be, for each P, approximately partitioned into a "discrete" spectrum of well separated points and a "quasi-continuum" concentrated near the set $\Omega^m_j(P) \in \mathcal{C} \equiv [-v_0\,P - \mathrm{i}\,v_0\,\mu_\mathrm{t}, v_0\,P - \mathrm{i}\,v_0\,\mu_\mathrm{t}]$, i.e., $\mu^m_j(P) = \mu_\mathrm{t}$ and $-v_0 \le v^m_j(P) \le v_0$. With the improving discretization (truncation $N\to\infty$), the quasi-continuum spectrum converges to the continuum set $\mathcal{C}$.

The quantities $\mu^m_j(P)$ and $v^m_j(P)$ in Eq. (45), computed with the medium parameters listed in Section 2 and with the RTE truncation[9] $N = 800$ are plotted in Fig. 8. As marked in the Figure, low-attenuation and low-velocity modes appearing for smaller P values (say, $P/\mu_\mathrm{t} < 1$) are responsible for the ordinary late-time diffusion. Early-time diffusion is associated with those high-P modes for which velocities approach the coherent wave velocity and which are still attenuated significantly less than the coherent component.

The crucial feature of the spectrum is that its discrete component persists only up to a certain maximum P value, estimated [1] as $P_\mathrm{max} \sim (k_0\,a)^2$; in our case $P_\mathrm{max} \sim 2500$. Beyond that P value all the modes belong to the continuum and are attenuated at the same rate as the coherent wave.

The point-spread function (Section 4) is expressed in terms of the radiance (11), which, according to Eqs. (36), (38), and (43), takes the form of the partial-wave expansion

$$I(t,R,\cos\theta) = \sum_{l=0}^{\infty}\sqrt{2l+1}\;\mathrm{P}_l\big(\cos\theta\big)\;I_l(t,R) \quad \textbf{(46)}$$

with the coefficients[10]

$$\begin{aligned} I_l(t,R) = \frac{v_0}{2\pi^2}\int_0^\infty \mathrm{d}P\,P^2\sum_j \mathrm{e}^{-\,\mathrm{i}\,\Omega^0_j(P)\,t}\,\mathrm{i}^l\,\mathrm{j}_l(PR) \\ w^0_{j,0}(P)\,w^0_{j,l}(P)\,, \end{aligned} \quad \textbf{(47)}$$

where the spherical Bessel functions result from a decomposition of a plane wave into spherical harmonics and from angular integration.

In reality, the transmitted intensity pulse always has a finite time duration; for example, it may be a Gaussian (9a) of width T_p. The observed radiance is then the convolution $I\circ A$ of the radiance (46) with the pulse profile A. That convolution, in turn, is equivalent to introducing in the integral (47) a window (or a low-pass filter), effectively limiting the P integration to $P/\mu_\mathrm{t} \lesssim \ell_\mathrm{t}/(v_0\,T_\mathrm{p})$. The window corresponding to $T_\mathrm{p} = 0.002\,\ell_\mathrm{t}/v_0$, hence $P/\mu_\mathrm{t} \lesssim 500$, is shown by the dashed lines in Figs. 8. In this case the P cutoff is high enough to include essentially all the ETD contributions; further shortening of the transmitted pulse has practically no effect, since it only adds contributions attenuated at the rate of the coherent signal.

While distribution of the eigenvalues Ω^0_j mostly affects the time dependence of the radiance (46), its *angular* dependence is controlled by the behavior of the components of the eigenvectors w^0_j (Eq. (47)).

Fig. 9 shows partial-wave distributions of several eigenfunctions for small P (contributing to the late-time diffusion) and for large P (contributing to the ETD signal). The plots show that, for each P, the eigenvector components decay with l nearly exponentially, but with P-dependent slopes.

Another way of assessing the angular dependence of radiance is to consider the individual partial-wave contributions (47). In Fig. 10 we plot, in the time range comparable to the estimated ETD time scale (6), the coefficients $I_l(t,R)$ convolved with the transmitted pulse (9a), as appearing in Eq. (16). The low partial waves have a smooth time dependence characteristic of late-time diffusion. In

[9] Results for higher truncation values are visually almost identical, except that the width of the "quasi-continuum band" in $\mu^m_j(P)/\mu_\mathrm{t}$ decreases approximately as $\sim 1/N$.

[10] These coefficients are identical to J_l defined in [2], Eq. (8), for a delta-function source, $A(t) = \delta(t)$.

particular, the $l = 0$ coefficient is very small in the considered time range and becomes large only in the late-time diffusion regime, $(v_0 t - R)/\ell_t > 1$ and $(v_0 t - R)/\ell_t \gg 1$. As l increases, the functions $I_l(t, R)$ rise with time more and more steeply and, for sufficiently large l, also decay more rapidly with t. In other words, high-l contributions to radiance become entirely concentrated in the ETD time range.

We note here that the individual partial-wave components of the radiance are not constrained to be non-negative; the non-negativity condition applies only to the total radiance (46), and holds for the results of our computations.

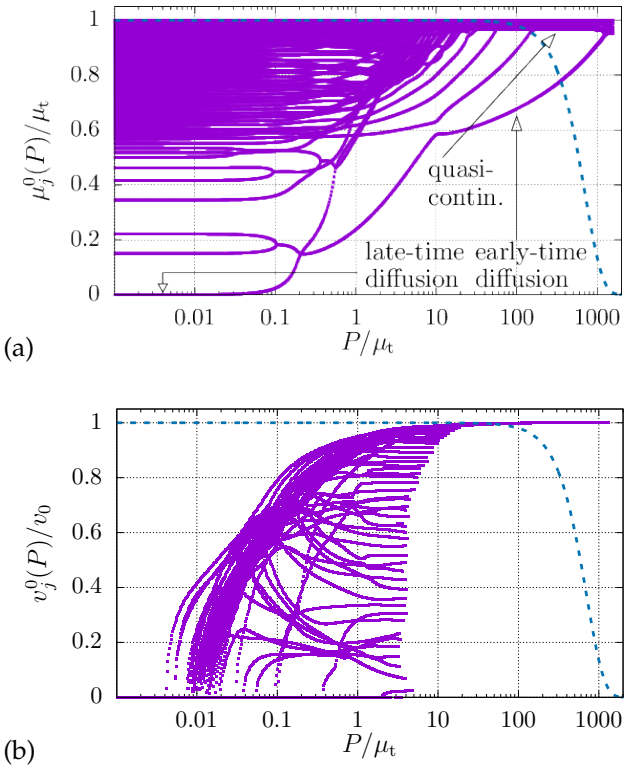

Fig. 8. Eigenvalues of attenuation coefficients and propagation velocities (45) of the RTE modes, relative to the corresponding quantities for the coherent wave propagation. Dashed curves represent the window in the integration variable P, due to the transmitted pulse (9a) of duration $T_p = 0.002\,\ell_t/v_0$.

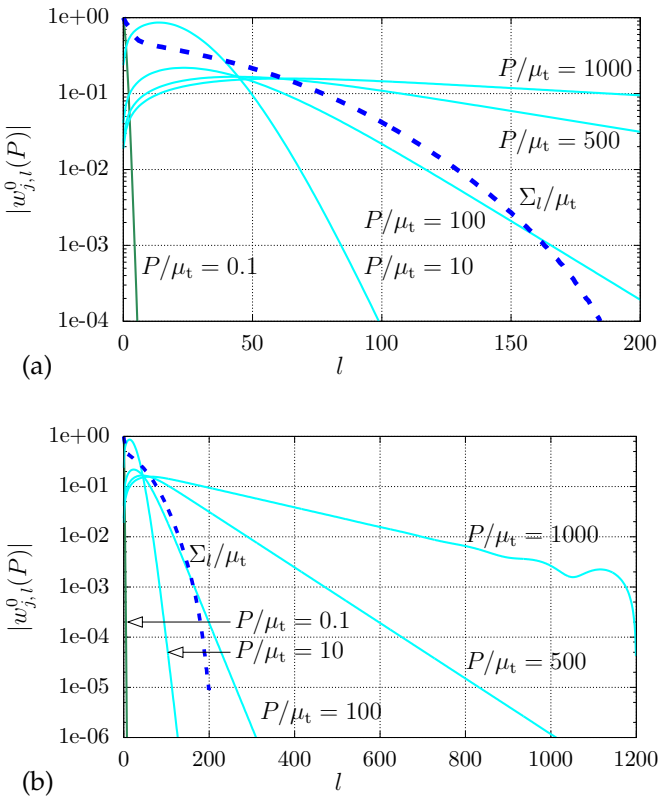

Fig. 9. Partial-wave components of leading modes for the indicated P values, compared to the behavior of the scattering kernel Σ_l. The plots (a) and (b) show, respectively, the lower- and higher-l components of the eigenvectors. The RTE is truncated at $N = 1200$.

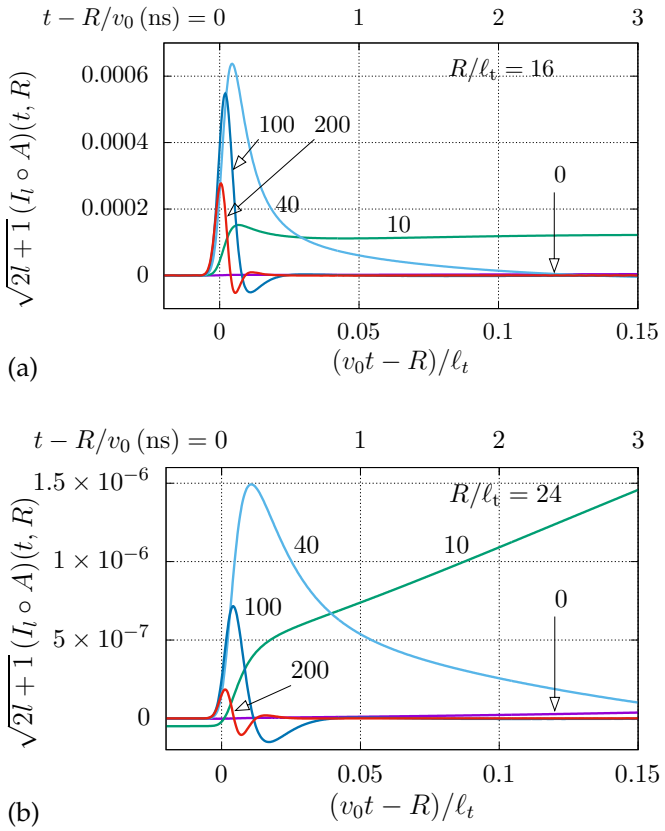

Fig. 10. Time dependence of the partial-wave coefficients (47) convolved with a short transmitted pulse $A(t)$ of width $T_p = 0.002\,\ell_t/v_0$, for $R/\ell_t = 16$ (a) and $R/\ell_t = 24$ (b), for the indicated angular momenta $l = 0, 10, 40, 100, 200$. The coefficient for $l = 0$ is very small in the considered time interval and becomes sizable only for $(v_0 t - R)/\ell_t > 1$, i.e., in the late-time diffusion regime.

REFERENCES

1. E. Bleszynski, M. Bleszynski, and T. Jaroszewicz, "Early-time diffusion in pulse propagation through dilute random media," Opt. Lett. **39**, 5862–5865 (2014).
2. E. Bleszynski, M. Bleszynski, and T. Jaroszewicz, "Enhancing early-time diffusion through beam collimation in pulse propagation in sparse discrete random media," Opt. Lett. **43**, 3762–3765 (2018).
3. S. Chandrasekhar, *Radiative Transfer* (Dover, New York, 1960).
4. G. C. Pomraning, "The Fokker-Planck operator as an asymptotic limit," Math. Model. Methods Appl. Sci. **2**, 21–36 (1992).
5. G. C. Pomraning, "Higher order Fokker-Planck operators," Nucl. Sci. Eng. **124**, 390–397 (1996).
6. C. L. Leakeas and E. W. Larsen, "Generalized Fokker-Planck approximations of particle transport with highly forward-peaked scattering," Nucl. Sci. Eng. **137**, 236–250 (2001).
7. A. P. Prudnikov, Y. A. Brychkov, and O. I. Marichev, *Integrals and Series. Vol. 2: Special Functions* (Gordon and Breach, 1986).
8. F. W. J. Olver, D. W. Lozier, R. F. Boisvert, and C. W. Clark, eds., *NIST Handbook of Mathematical Functions* (Cambridge University Press, 2010).
9. A. N. Tikhonov and V. Y. Arsenin, *Solutions of Ill-Posed Problems* (V. H. Winston & Sons, Washington, DC, 1977).
10. J.-L. Starck, E. Pantin, and F. Murtagh, "Deconvolution in astronomy: A review," Publ. Astron. Soc. Pac. **114**, 1051–1069 (2002).
11. K. M. Case and P. F. Zweifel, *Linear Transport Theory*, Addison-Wesley Series in Nuclear Science and Engineering (Addison-Wesley, Reading, MA, 1967).
12. A. Ishimaru, *Wave Propagation and Scattering in Random Media* (John Wiley, 1999).
13. L. Ryzhik, G. Papanicolaou, and J. B. Keller, "Transport equations for elastic and other waves in random media," Wave Motion **24**, 327–370 (1996).

APPENDIX C (ICEAA 2018)

Early-time diffusion in imaging through obscuring random media: two-way propagation and deblurring

Elizabeth Bleszynski
Monopole Research
739 Calle Sequoia
Thousand Oaks, CA 91360
elizabeth@monopoleresaerch.com

Marek Bleszynski
Monopole Research
739 Calle Sequoia
Thousand Oaks, CA 91360
marek@monopoleresaerch.com

Thomas Jaroszewicz
Monopole Research
739 Calle Sequoia
Thousand Oaks, CA 91360
tomek@monopoleresaerch.com

***Abstract*—The radiative transport theory predicts that a short pulse propagating through a random medium consisting of discrete scatterers of sizes large compared to the wavelength develops to develop an "early-time diffusion" (ETD) component: a sharply rising structure in the time-resolved intensity, immediately following the coherent (ballistic) signal, but attenuated at a rate substantially lower than the coherent attenuation. This phenomenon offers a possibility of application in imaging through obscuring (e.g., atmospheric) media. We describe here an imaging scenario utilizing the ETD signal, evaluate the resulting point-spread function characterizing the image resolution, and show how that resolution can be significantly improved by means of regularized deconvolution techniques.**

***Index Terms*—propagation, random medium, imaging radiative transfer**

I. Introduction

We have previously identified [1] an interesting behavior of solutions of the time-dependent radiative transport equation (RTE) describing propagation of short pulses in a discrete-scatterer medium: if scatterers are large compared to the wavelength, the time-resolved intensity develops a sharply rising structure immediately following the coherent (ballistic) signal but attenuated at a significantly lower rate.

In this note we concentrate on the angular distribution of the energy flux associated with the ETD components of the radiance and on the problem of the angular resolution in imaging based on the ETD signals. The main envisaged applications include imaging through particulate obscuring atmospheric media, such as fog, mist, and aerosols; however, a closely similar approach can be applied to laboratory-scale imaging: medical, fuel-combustion, etc.

We show that the image point-spread function (PSF) obtained from the RTE solutions contains a significant amount of Fourier components higher than θ_0^{-1} (θ_0 being the width of the forward scattering peak in the medium constituent cross-section). Those components can be enhanced by an appropriate regularized deconvolution, leading to a substantial angular resolution improvement, typically by the factor of 3 of 4 for propagation through the distance of about 20 mean free paths.

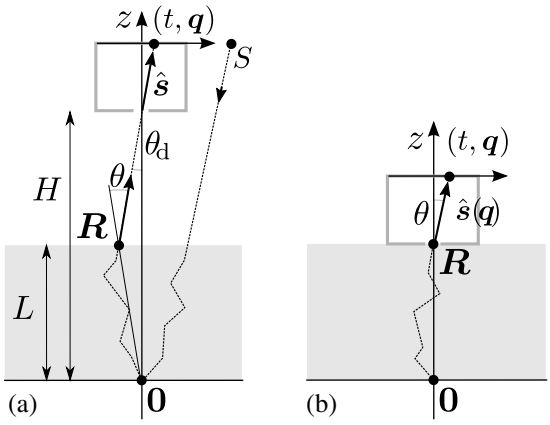

Fig. 1: A schematic representation of the considered imaging scenario (a) and a simpler propagation problem (b), with greatly exaggerated deviations of the light propagation path from the straight line.

II. The imaging scenario and simple estimates

We discuss here, for conceptual simplicity, a non-scanning imaging scenario (Fig. 1), in which a fairly large part of the scene is illuminated by a wide pulsed beam emitted by a source S and the image is taken by a camera, understood as an array of sensors recording time-resolved intensity.[1]

For definiteness, we consider a flat scene covered by a layer of an obscuring medium (such as fog, smoke, or other aerosol) of thickness L. In the assumed active optical imaging scenario (Fig. 1(a)) the pulsed beam source and the detector is located at the height H directly above the objects(s) of interest.[2]

[1] It is straightforward to show that this scheme results in the same angular resolution as a more practical scanning imaging, in which a narrow pulsed beam moves across the scene, illuminates individual patches, and the reflected light is registered by a "single-pixel camera", i.e., an optical sensor collecting light from a large angular field of view.

[2] The above assumptions are made for simplicity only; our treatment can be easily generalized to a medium layer located above the scene and to a slanted-view geometry.

In the above scenario the illuminating pulsed beam passes through the medium layer and undergoes scattering, which causes its spread in time.[3] Nevertheless, the evolved pulse will always contain a short rise-time ETD signal. Next, the incident pulse scatters from the scene and that scattering

In the optical domain, most objects of interest are diffuse scatterers; therefore, reflecting points on the scene can be considered secondary, practically omnidirectional intensity sources, re-emitting the incident pulses. The reflected pulse due to a scatterer located at the origin (Fig. 1(a)) propagates through the medium layer and undergoes further scattering, until it emerges from the layer's upper boundary. After traveling along a straight line through the camera lens it forms a focal-plane intensity image, identified with the point-spread function (PSF) characterizing effects of the medium. In that image, distances of pixel locations from the optical axis of the camera are approximately proportional to the pulse arrival angle $\theta_{\rm d}$.

For simplicity, we will only discuss angular flux distributions at the upper boundary of the medium layer and described them in terms of the angle θ (Fig. 1(a)); these distributions are independent of the camera location H. Because of the relation $\theta_{\rm d} \approx (R/H)\,\theta$, the actual resolution of the camera can only be better than the resolution for the camera located just above the medium layer (Fig. 1(b)).

In the calculations reported here we assume parameters typical of optical propagation through a cloud, fog, or mist: $\lambda_0 = 0.633\,\mu$m, $a = 5\,\mu$m $\approx 8\,\lambda_0$, hence $k_0\,a \equiv 2\pi a/\lambda_0 \approx 50$ and the forward peak in scattering on a single droplet has the width $\theta_0 \approx 1/(k_0 a) \approx 0.02\,$rad. The assumed number density of water droplets is $n_0 = 10^{-6}\,{\rm m}^{-3}$, resulting in a relatively short mean-free path[4] $\ell_{\rm t} \approx 6\,$m. In our examples of propagation through the distance $R = 24\,/\ell_{\rm t}$ the estimated [1] temporal width of the ETD signal is $\Delta t_{\rm ETD}(R) \approx 0.4\,$ns, much less than the time scale $\ell_{\rm t}/v_0 \approx 20\,$ns of the ordinary, late-time diffusion (LTD). Accordingly, we will consider transmitted pulses shorter than the ETD time scale, typically of duration $T_{\rm t} \lesssim 0.1\,$ns, and in isolating the ETD signal (as described below), we will use filters of temporal width $T_{\rm f}$ somewhat larger than the ETD time scale and much smaller than the LTD time scales.

III. Solution of the RTE and the Point-Spread Function

The RTE [2]–[5] for the coordinate space Green function Γ can be written in the standard form

$$\left(\mu_{\rm t} + v_0^{-1}\,\partial_t + \hat{\boldsymbol{s}}\cdot\boldsymbol{\nabla}_{\boldsymbol{R}}\right)\Gamma(t,\boldsymbol{R};\hat{\boldsymbol{s}},\hat{\boldsymbol{s}}') \qquad (1)$$
$$-\int {\rm d}^2\hat{s}''\,\Sigma(\hat{\boldsymbol{s}}\cdot\hat{\boldsymbol{s}}'')\;\Gamma(t,\boldsymbol{R};\hat{\boldsymbol{s}}'',\hat{\boldsymbol{s}}') = \delta(t)\,\delta^3(\boldsymbol{R})\,\delta^2(\hat{\boldsymbol{s}}-\hat{\boldsymbol{s}}')\,;$$

[3] The scattering-induced angular spread is small compared to the assumed already wide beam, and practically does not affect scene illumination.

[4] This quantity is given by $\ell_{\rm t} = 1/(n_0\,\sigma_{\rm t})$, where n_0 is the medium number density and $\sigma_{\rm t}$ the ensemble-averaged total cross-section on a single medium constituent.

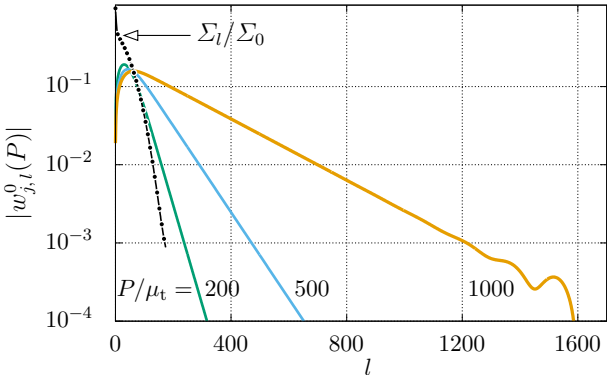

Fig. 2: Partial-wave components of leading discrete-spectrum modes for the indicated P values, compared to the behavior of the scattering kernel Σ_l. The RTE is truncated at $N = 1600$.

here $\Gamma(t,\boldsymbol{R};\hat{\boldsymbol{s}},\hat{\boldsymbol{s}}')$ is the radiance at the observation point $(t,\boldsymbol{R})$ due an infinitely short pulse emitted at the time $t = 0$ from the origin $\boldsymbol{R} = \boldsymbol{0}$ in the direction $\hat{\boldsymbol{s}}$.

A practical solution of the RTE involves decomposition of the Green function in plane waves of frequencies Ω and wave vectors $\boldsymbol{P}$, $\exp(-{\rm i}\,\Omega\,t)\,\exp({\rm i}\,\boldsymbol{P}\cdot\boldsymbol{R})$, and its decomposition, as a function of flux directions $\hat{\boldsymbol{s}}$ and $\hat{\boldsymbol{s}}'$, in rotated spherical harmonics $\mathrm{Y}_{l,m}(\hat{\boldsymbol{s}};\hat{\boldsymbol{P}})$ and $\mathrm{Y}^*_{l',m}(\hat{\boldsymbol{s}}';\hat{\boldsymbol{P}})$ defined relative to the direction of the wave number. In this representation, expansion coefficients of the Green function, truncated to $l,l' < N$, can be expressed in terms of the frequency eigenvalues $\Omega^m_j(P)$, indexed with $j = 1,2,\ldots N$ and the corresponding eigenvectors $w^m_j(P)$, whose components are labeled with $l = 0,1,\ldots,N-1$.

As can be seen from the form of the plane-wave expansion, the imaginary parts of the frequency eigenvalues are proportional to attenuation coefficients $\mu^m_j(P) = -\,{\rm Im}\,\Omega^m_j(P)/v_0$ of the radiance modes and their real parts are related to the modes' propagation velocities $v^m_j(P) = {\rm Re}\,\Omega^m_j(P)/P$. As discussed in [1], low-attenuation modes appearing for smaller P values (say, $P/\mu_{\rm t} < 1$) are responsible for the ordinary late-time diffusion; these modes are also characterized by nearly zero velocities. Early-time diffusion is associated with those high-P modes for which velocities approach the coherent wave velocity and which are still attenuated significantly less than the coherent component.

Fig. 2 shows partial-wave distributions of several eigenfunctions for large P (contributing to the ETD signal). The plots show that the eigenvector components decay with l nearly exponentially, but more and more higher l values are present with increasing P, very significantly exceeding the range of angular momenta present in the scattering cross-section (the coefficients Σ_l); this fact will be crucial in the deconvolution procedure (Sec. IV).

The PSF obaserved by the camera (Fig. 1) is expressible in terms of the time- and angle-resolved intensity at the observation point $\boldsymbol{R}$, due to the considered instantaneous (proportional to $\delta(t)$) pulse emitted from the point $\boldsymbol{0}$; because of diffuse scattering from the scene, the emitted pulse may be

assumed omnidirectional. The PSF is thus related to the RTE Green function integrated over the initial flux directions,

$$I_0(t, |\boldsymbol{R}|, \hat{\boldsymbol{R}} \cdot \hat{\boldsymbol{s}}) = \int \mathrm{d}^2 \hat{s}' \, \Gamma(t, \boldsymbol{R}; \hat{\boldsymbol{s}}, \hat{\boldsymbol{s}}') \, ; \tag{2}$$

by invariance of the RTE, the intensity I_0 is a function of only the distance $R = |\boldsymbol{R}|$ and the cosine of the angle θ.

In order to specify the PSF as an image formed on the focal plane, we must map the pulse arrival direction $\hat{\boldsymbol{s}}$ (parameterized in terms of the polar angle θ and the corresponding azimuthal angle ϕ) to a point $\boldsymbol{q}(\hat{\boldsymbol{s}})$ (Fig. 1(b)). It will be convenient to calibrate the coordinates $q(\hat{\boldsymbol{s}})$ such that $|\boldsymbol{q}(\hat{\boldsymbol{s}})| \approx \theta$ for $\theta \ll 1$. A uniquely appropriate mapping turns out to be

$$\cos\theta(q) = 1 - \tfrac{1}{2}\, q^2 \, , \tag{3}$$

meant to be an *exact* expression, and not a small-angle approximation.

Now we simply *define* an interim *time-dependent* axially symmetric PSF as the intensity (2) with θ expressed in terms of q; in an ad-hoc notation, we set

$$\Upsilon(t, R; q) := I_0(t, R, \cos(\theta(q))) \equiv I_0\big(t, R, 1 - \tfrac{1}{2}\, q^2\big) \, . \tag{4}$$

With the RTE solution given by the eigenmode representation, the radiance I_0 and thus the time-dependent PSF

$$\begin{aligned} \Upsilon(t, R, q) &= \frac{v_0}{2\pi^2} \int_0^\infty \mathrm{d}P \, P^2 \sum_j \mathrm{e}^{-\mathrm{i}\, \Omega_j^0(P)\, t} \, w_{j,0}^0(P) \\ &\qquad \sum_{l=0}^{\infty} \sqrt{2l+1}\, \mathrm{i}^l \, \mathrm{j}_l(PR)\, \mathrm{P}_l\big(1 - \tfrac{1}{2}\, q^2\big)\, w_{j,l}^0(P) \, , \\ &\equiv \sum_{l=0}^{\infty} \mathrm{P}_l\big(1 - \tfrac{1}{2}\, q^2\big)\, \Upsilon_l(t, R) \end{aligned} \tag{5}$$

are expressed in terms of the RTE eigenvalues and eigenvectors.

The time-dependent basic PSF specified above is due to an infinitely short emitted pulse, i.e., a source proportional to the delta function in time.

However, in the considered imaging scenario discussed in Section II the transmitted pulse of time profile $S_0(t)$ and a certain initial angular spread travels the distance R to the scene and evolves to become a stretched in time pulse $S_R(t)$, whose time-dependence depends also on the angular width w of the emitted beam.

By assuming a Gaussian angular beam source distribution defined, in image coordinates, by $B(\boldsymbol{q}) = \mathrm{e}^{-\,q^2/2w^2}/(2\pi w^2)$ we can express the evolved pulse profile $S_R(t)$ as the source convolution with the same as before basic PSF (4).

Now the actual measured time-dependent PSF is the convolution $\big(\Upsilon(\cdot, R; q) \circ S_R(\cdot)\big)(t)$ of the evolved pulse illuminating the scene and the PSF (4) due to signal propagation from the scene to the detector. Both of these functions involve temporal pulse spreading due to diffusion, and that spreading can be removed by applying an appropriate high-pass filter Φ [1]. The result of the filtering can be represented as

$$\begin{aligned} \Upsilon_\Phi(t, R; q) &= \big(\Phi \circ \Upsilon(\cdot, R; q) \circ S_R(\cdot)\big)(t) \\ &\equiv \int \mathrm{d}t' \int \mathrm{d}t'' \, \Phi(t - t') \, \Upsilon(t' - t'', R; q) \, S_R(t'') \, . \end{aligned} \tag{6}$$

The above quantity is, generally, not positive-definite; therefore, we define the final time-independent, non-negative PSF Λ by taking the absolute value of $\Upsilon_\Phi(t, R; q)$ and integrating it over a time interval containing its peak. The integration limits t_1 and t_2 can be automatically determined on the basis of the shape of the filtered signal, without any a-priori knowledge of the arrival time of the pulse. The proposed prescription for the PSF (and, generally, for image formation) is thus

$$\Lambda_\Phi(R; q) = \int_{t_1}^{t_2} \mathrm{d}t \, \big|\Upsilon_\Phi(t, R; q)\big| \, . \tag{7}$$

IV. The deblurring procedure

A widely used approach to improving resolution of images is based on deconvolution with Tikhonov-type regularization (e.g., [6], [7]).

In the considered optical imaging scenario, linearity of the measured image intensity in the objects' reflectivity implies that the observed image is given by the convolution

$$F(\boldsymbol{q}) = \big(\Lambda \circ f\big)(\boldsymbol{q}) + \eta(\boldsymbol{q}) \, , \tag{8}$$

where f is the ideal image (object) function, Λ is the PSF, and η a random function representing an additive noise.

In practice, convolutions such as in Eq. 8 are performed in Fourier space, where they become products of Fourier transforms. A very useful property of our mapping (3) is that it provides a simple relation between the those Fourier (or Hankel) transforms of the PSF and the partial-wave coefficients in Eq. (5),

$$\begin{aligned} \widetilde{\Upsilon}(t, R; \varrho) &:= 2\pi \int_0^\infty \mathrm{d}q \, q \, \mathrm{J}_0(q\varrho)\, \Upsilon(t, R; q) \\ &= \sum_{l=0}^{\infty} D_l(\varrho)\, \Upsilon_l(t, R) \, , \end{aligned} \tag{9}$$

with closed-form coefficients

$$D_l(\varrho) = \frac{4\pi}{\varrho} \, \mathrm{J}_{2l+1}(2\varrho) \, , \tag{10}$$

strongly peaked at $\varrho \approx l$. As a result, presence of high angular momenta l in the RTE eigenmodes (Fig. 2) implies presence of high Fourier transforms in the PSF.

Now, recovering the unknown ideal image amounts to solving the (usually ill-posed) Fourier-space inverse problem

$$\widetilde{\Lambda}(\boldsymbol{\varrho})\, \widetilde{f}(\eta; \boldsymbol{\varrho}) = \widetilde{F}(\boldsymbol{\varrho}) - \widetilde{\eta}(\boldsymbol{\varrho}) \tag{11}$$

with its "exact" r.h.s. $\widetilde{F}$ perturbed by the noise, hence the dependence of the solution f on η.

A naive inverse filtering procedure amounts to constructing

$$\widetilde{f}(\eta; \boldsymbol{\varrho}) = \frac{\widetilde{F}(\boldsymbol{\varrho}) - \widetilde{\eta}(\boldsymbol{\varrho})}{\widetilde{\Lambda}(\boldsymbol{\varrho})} \, ; \tag{12}$$

division by the Fourier-space PSF enhances large Fourier components of the observed image and improves the resolution. However, it is well known to fail in realistic problems because of the effects of noise. Since noise has, typically, a wide spectrum, its contribution to the expression (12) may, for large $|\boldsymbol{\varrho}|$, overwhelm the measured image data $\widetilde{F}(\boldsymbol{\varrho})$. In such

situations often an adequate solution is a simple regularized deconvolution

$$\widetilde{f}_\beta(\eta;\boldsymbol{\varrho}) = \frac{\widetilde{\Lambda}(\boldsymbol{\varrho})\,[\widetilde{F}(\boldsymbol{\varrho}) - \widetilde{\eta}(\boldsymbol{\varrho})]}{\widetilde{\Lambda}^2(\boldsymbol{\varrho}) + \beta^2} \tag{13}$$

with a real regularization parameter $\beta > 0$ [6], [7]. That parameter can be adjusted so that, depending on $\boldsymbol{\varrho}$, the noise contribution to $\widetilde{f}_\beta(\eta;\boldsymbol{\varrho})$ is much smaller than the signal or both η and F contributions are negligibly small.

To assess the resolution improvement achievable with the described regularized deconvolution, we apply it to the PSF itself and define the "deblurred PSF" by

$$\widetilde{\Lambda}_\beta(\eta;\boldsymbol{\varrho}) = \frac{\widetilde{\Lambda}(\boldsymbol{\varrho})\,[\widetilde{\Lambda}(\boldsymbol{\varrho}) - \widetilde{\eta}(\boldsymbol{\varrho})]}{\widetilde{\Lambda}^2(\boldsymbol{\varrho}) + \beta^2}\,. \tag{14}$$

To assess effects of this procedure, we apply it to the normalized modulation transfer function (MTF) $\widetilde{M}(\eta;\boldsymbol{\varrho}) := \widetilde{\Lambda}(\eta;\boldsymbol{\varrho})/\widetilde{\Lambda}(\eta;\mathbf{0})$ and express the result in terms of the dimensionless noise $\hat{\eta}(\boldsymbol{\varrho}) := \widetilde{\eta}(\boldsymbol{\varrho})/\widetilde{\Lambda}(\mathbf{0})$ and the dimensionless regularization parameter $\hat{\beta} := \beta/\widetilde{\Lambda}(\mathbf{0})$. Straightforward estimates show then that, if one takes $\hat{\beta}$ satisfying the conditions

$$|\hat{\eta}(\boldsymbol{\varrho})| \ll \hat{\beta} \ll 1\,, \tag{15}$$

the deblurred MTF,

$$\widetilde{M}_\beta(\eta;\boldsymbol{\varrho}) = \frac{\widetilde{M}(\boldsymbol{\varrho})\,[\widetilde{M}(\boldsymbol{\varrho}) - \hat{\eta}(\boldsymbol{\varrho})]}{\widetilde{M}^2(\boldsymbol{\varrho}) + \hat{\beta}^2}\,, \tag{16}$$

is immune to noise.

As an example, the original MTF and the deconvolution result $\widetilde{M}_\beta(\eta;\boldsymbol{\varrho})$ are plotted in Fig. 3 for the propagation distance $R = 24\,\ell_\mathrm{t}$. The original MTF clearly exhibits a long tail which can be shown to be dominated by the coherent contributions to the radiance. We assume here the noise η_0 at the level of the asymptotic large-$\boldsymbol{\varrho}$ contribution to the MTF, which means that the coherent component of the image is, in practice, unobservable. Correspondingly, we took $\hat{\beta} = 10^{-3}$, about 10 times higher than the assumed noise level. It is seen that the values of the deblurred MTF stay close to 1 in a considerable range of q values, hence a significant resolution improvement can be expected.

This expectation is confirmed in Fig. 4 which show the original PSF $\Lambda(\boldsymbol{q})$ and the "deblurred PSF", i.e., the absolute value of the inverse Fourier transform $M_\beta(\eta;\varrho)$ of the function $\widetilde{M}_\beta(\eta;\varrho)$, both normalized to their values at $q = 0$. It is evident that the distribution of M_β is significantly narrower than that of Λ and the differential cross-section σ – a finding that may further improve the prospects of application of ETD phenomena in imaging.

Acknowledgment

This material is based upon work supported by the U. S. Air Force Office of Scientific Research under award number FA 9550-16-C-0014.

References

[1] E. Bleszynski, M. Bleszynski, and T. Jaroszewicz, "Early-time diffusion in pulse propagation through dilute random media," *Optics Letters*, vol. 39, no. 20, pp. 5862–5865, 2014.

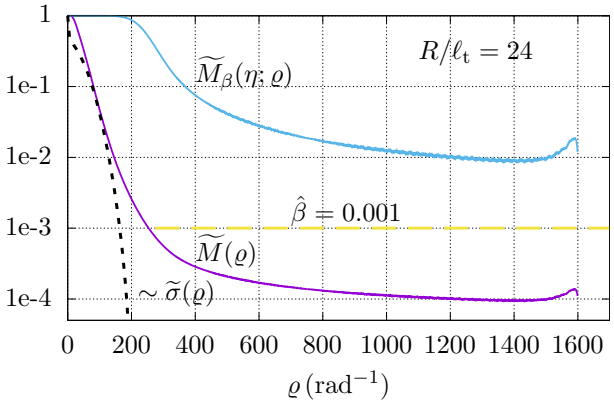

Fig. 3: MTFs, original and after deconvolution, for the medium layer thickness $R = 24\,\ell_\mathrm{t}$. The indicated value of the regularization parameter $\hat{\beta}$ shows that the deconvolution is immune to noise at the level of the coherent component of the signal. The shape of the Fourier transform of the scattering cross-section is plotted for comparison.

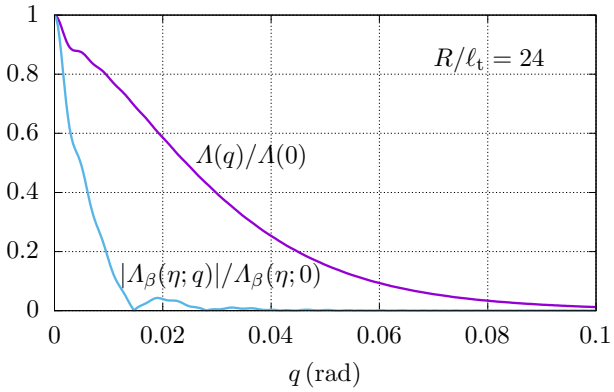

Fig. 4: Original and deblurred PSFs for the layer thickness $R = 24\,\ell_\mathrm{t}$. The FWHM width of the deblurred PSF is, approximately, 0.010 radians.

[2] S. Chandrasekhar, *Radiative Transfer*. New York: Dover, 1960.

[3] K. M. Case and P. F. Zweifel, *Linear Transport Theory*, ser. Addison-Wesley Series in Nuclear Science and Engineering. Reading, MA: Addison-Wesley, 1967.

[4] A. Ishimaru, *Wave Propagation and Scattering in Random Media*. John Wiley, 1999.

[5] L. Ryzhik, G. Papanicolaou, and J. B. Keller, "Transport equations for elastic and other waves in random media," *Wave Motion*, vol. 24, pp. 327–370, 1996.

[6] A. N. Tikhonov and V. Y. Arsenin, *Solutions of Ill-Posed Problems*. V. H. Winston & Sons, Washington, DC, 1977.

[7] J.-L. Starck, E. Pantin, and F. Murtagh, "Deconvolution in astronomy: A review," *Publications of the Astronomical Society of the Pacific*, vol. 114, no. 800, pp. 1051–1069, 2002.

APPENDIX D (EUCAP 2017)

Reduction of Singular Surface Integrals to Non-Singular Line Integrals for Matrix Elements of Tensor and Vector Green Functions in Integral Equations Involving Non-Parallel Surface Elements

Elizabeth Bleszynski*, Marek Bleszynski*, Thomas Jaroszewicz*,
*Monopole Research, Thousand Oaks, CA 91360
* email address: elizabeth@monopoleresearch.com

***Abstract*—We consider an approach allowing conversion of surface integrals (over planar surface elements) to line integrals, in evaluating matrix elements of Helmholtz-equation Green function and its derivatives, in particular the vector Green function in electromagnetics. A general procedure is outlined consisting of finding suitable auxiliary functions applicable to particular kernel operators and explicit expressions are provided in the static limit. In the latter case, the accuracy and the computational cost of the proposed technique are compared to those of conventional approach based on evaluating surface integrals with the conventional singularity extraction method.**

***Index Terms*—Integral equations, Moment methods, Numerical analysis**

I. Introduction

In our recent paper [1] we presented a procedure for the evaluation of matrix elements of the kernels of surface integral equation operators – the tensor and the vector Green functions – sandwiched between the surface Rao-Wilton-Glisson (RWG) [2] basis functions defined on parallel triangular supports. In contrast to the majority of methods [3] used in computation of matrix elements of singular Green functions, i.e., singularity subtraction (e.g., [4]) and singularity cancellation (e.g., [5], [6], [7] techniques), our procedure consisted of converting four-dimensional surface integrals with singular integrands to two-dimensional line integrals involving auxiliary non-singular functions. The most essential element of the procedure consisted of employing a representation of the Green function of the scalar Helmholtz equation,

$$g(k,R)=\frac{\mathrm{e}^{\,\mathrm{i}\,kR}}{4\pi R}\,, \tag{1}$$

in terms of an auxiliary, non-singular function $m(\xi)=\sum_{p=1}^{\infty}\frac{\xi^p}{p\,p!}$,

$$g(k,|\boldsymbol{R}|)=-\frac{1}{4\pi\mathrm{i}k}\,\boldsymbol{\nabla}^{(2)}_{\boldsymbol{R}}\cdot\boldsymbol{\nabla}^{(2)}_{\boldsymbol{R}}\,m(\mathrm{i}k\,|\boldsymbol{R}|)\,, \tag{2}$$

where

$$\boldsymbol{\nabla}^{(2)}_{\boldsymbol{R}}=\hat{\boldsymbol{n}}\times(\boldsymbol{\nabla}^{(3)}_{\boldsymbol{R}}\times\hat{\boldsymbol{n}}) \tag{3}$$

are gradients in the plane of the considered triangular patches T_1 and T_2, expressed in terms of the unit vector normal $\hat{\boldsymbol{n}}$ to that plane and the three-dimensional gradient $\boldsymbol{\nabla}^{(3)}_{\boldsymbol{R}}$. The representation (2) allowed us to convert, by making use of the Gauss divergence theorem, the integral over the surfaces of two triangles to line integrals, with regular integrands, over triangle edges.

In the subsequent paper [8], we considered an extension of our method to problems involving non-planar geometries. The essence of our approach was to generalize the representation (2) of the Green function to non-parallel geometry elements: the new representation involves a bilinear form of two gradient operators $\boldsymbol{\nabla}_1$ and $\boldsymbol{\nabla}_2$ ***acting in two different, non-parallel, planes***, $\mathit{\Pi}_1$ and $\mathit{\Pi}_2$, containing the triangles T_1 and T_2. Specifically, we determined a function $\mathit{\Phi}^{(1)}$ such that, schematically,

$$g\big(k,|\boldsymbol{R}_1-\boldsymbol{R}_2|\big)=\big\{\boldsymbol{\nabla}_1\cdot[\,\hat{M}_a\,\boldsymbol{\nabla}_2\,]\big\}\,\mathit{\Phi}^{(1)}(k,a,\boldsymbol{R}_1-\boldsymbol{R}_2)\,, \tag{4}$$

where $\hat{M}_a$ is a suitably constructed (2×2) diagonal matrix (Eq. (11) below) dependent on the "inclination parameter"

$$a=\sin^2\theta\le\tfrac{1}{2}\,, \tag{5}$$

2θ being the angle between the planes $\mathit{\Pi}_1$ and $\mathit{\Pi}_2$ (Fig. 1).

The representation (4), in which the auxiliary function $\mathit{\Phi}^{(1)}(k,a,\boldsymbol{R}_1-\boldsymbol{R}_2)$ is a counterpart of the function m in Eq. (2), allows us, by proceeding along similar lines as in [1], to convert the double surface integral of the scalar Green function (as well as as all integrals appearing in the matrix elements of the tensor Green function sandwiched between two RWG basis functions) over two flat ***non-coplanar*** triangles $T_1\subset\mathit{\Pi}_1$ and $T_2\subset\mathit{\Pi}_2$ to the line integral over surfaces' perimeters,

$$\begin{aligned}&\int_{T_1}\mathrm{d}S_1\int_{T_2}\mathrm{d}S_2\;g(k,|\boldsymbol{R}_1-\boldsymbol{R}_2|)\\&=\oint_{\partial T_1}\mathrm{d}l_1\oint_{\partial T_2}\mathrm{d}l_2\,\big\{\hat{\boldsymbol{u}}_1\cdot[\,\hat{M}\,\boldsymbol{u}_2]\big\}\;\mathit{\Phi}^{(1)}(k,a,\boldsymbol{R}_1-\boldsymbol{R}_2)\,,\end{aligned} \tag{6}$$

with $\hat{\boldsymbol{u}}_1$ and $\hat{\boldsymbol{u}}_2$ representing unit vectors perpendicular to the perimeter lines, located in the planes $\mathit{\Pi}_1$ and $\mathit{\Pi}_2$.

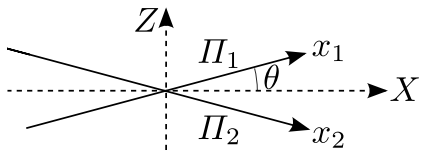

Fig. 1: Geometry of two intersecting planes, Π_1 and Π_2, defining "local" coordinates $(x_i, y_i) = \boldsymbol{r}_i \in \mathbb{R}^2$ and "global" coordinates $(X_i, Y_i, Z_i) = \boldsymbol{R}_i \in \mathbb{R}^3$. The y-axes of the three systems coincide, hence $y_1 = y_2 = Y_1 = Y_2$.

In the present paper we describe a procedure for constructing a set of auxiliary functions which allow us to convert expressions for matrix elements of both tensor and vector Green functions from surface line integrals.. The final result for matrix elements are given in terms of line integrals over triangle perimeters with simple and nonsingular integrands. The line integrals can be further evaluated analytically. However, the computation cost of evaluating the obtained analytical expression may be comparable to the cost of quadratures.

II. The general approach

We list below the elements of our approach, combined with brief comments on the role they play in the complete derivation of the result for the vector Green function.

Our procedure consists of the following steps:

- Choice of a suitable Cartesian coordinate system defined by three mutually orthonormal vectors, with the axis $\hat{\boldsymbol{Y}}$ along the line of intersection of the planes Π_1 and Π_2 (Fig. 1). In this coordinate system we denote the vector representing the difference of two positions on the individual triangles with

$$\boldsymbol{R}_1 - \boldsymbol{R}_2 \equiv \boldsymbol{R} = (X, Y, Z) \tag{7}$$

(with few exceptions, we denote global coordinates with capitals, and the coordinates in the local systems of the planes Π_1 and Π_2 with lower-case letters).
The local coordinates $\boldsymbol{r}_i = (x_i, y_i)$ on the planes are mapped to the global coordinates by

$$\begin{aligned}\boldsymbol{R}_1(\boldsymbol{r}_1) &= (X_1, Y_1, Z_1) \\ &\equiv \left(\sqrt{1-a}\; x_1,\, y_1,\quad \sqrt{a}\; x_1\right)\end{aligned} \tag{8a}$$

and

$$\begin{aligned}\boldsymbol{R}_2(\boldsymbol{r}_2) &= (X_2, Y_2, Z_2) \\ &\equiv \left(\sqrt{1-a}\; x_2,\, y_2,\, -\sqrt{a}\; x_2\right),\end{aligned} \tag{8b}$$

hence

$$\begin{aligned}&\boldsymbol{R}(\boldsymbol{r}_1, \boldsymbol{r}_2) \equiv \boldsymbol{R}(\boldsymbol{r}_1) - \boldsymbol{R}(\boldsymbol{r}_2) \\ &= \left(\sqrt{1-a}\; (x_1 - x_2),\, y_1 - y_2, \sqrt{a}\; (x_1 + x_2)\right).\end{aligned} \tag{9}$$

The inverse mappings, $\boldsymbol{R} \longrightarrow \boldsymbol{r}_1$ and $\boldsymbol{R} \longrightarrow \boldsymbol{r}_2$ can be defined as

$$x_{\frac{1}{2}} = \pm\, \frac{X}{2\sqrt{1-a}} + \frac{Z}{2\sqrt{a}}\,, \quad y_{\frac{1}{2}} = \pm\, \frac{Y}{2}\,. \tag{10}$$

- Construction of the representation (4) for the scalar Green function of the Helmholtz equation $g(k, R)$, written more explicitly as

$$\begin{aligned}&\left\{\boldsymbol{\nabla}_{\boldsymbol{r}_1} \cdot [\hat{M}_a\, \boldsymbol{\nabla}_{\boldsymbol{r}_2}]\right\} \Phi^{(1)}(a, k; \boldsymbol{r}_1, \boldsymbol{r}_2) \\ &\equiv \left\{\partial_{x_1}\, \partial_{x_2} + (1-a)\, \partial_{y_1}\, \partial_{y_2}\right\}\, \Phi^{(1)}(a, k; \boldsymbol{r}_1, \boldsymbol{r}_2) \\ &= g(k; \boldsymbol{r}_1, \boldsymbol{r}_2)\,,\end{aligned} \tag{11}$$

where $\hat{M}_a = \mathrm{diag}(1, 1-a)$ and where it is understood that the Green function on the r.h.s. depends on the planar coordinates $\boldsymbol{r}_i$ through the relations (8).
The representation (11) allows us to reduce the four-dimensional surface integral over triangular facets to line integrals, with regular integrands, over perimeters of the triangular facets (Eq. (6)).
In the analysis of the vector Green function we will use Eq. (11) generalized to the gradient of the Green function g and to the square of the considered differential operator.
- Because of the relations (10), the differential operator in Eq. (11) can be also expressed in terms of the variables $\boldsymbol{R} = (X, Y, Z) \equiv (\boldsymbol{\rho}, s)$. Further, the coefficients in Eq. (11) were chosen to make the differential operator defined there invariant under rotations about the Z axis, and hence expressible in terms of $\rho = |\boldsymbol{\rho}| = \sqrt{X^2 + Y^2}$ and s only. Consequently, the function $\Phi^{(1)}$ depends also only on ρ and s, such that $\Phi^{(1)}(a, k; \boldsymbol{r}_1(\boldsymbol{R}), \boldsymbol{r}_2(\boldsymbol{R})) \equiv \widehat{\Phi}^{(1)}(a, k; \rho, s)$. In these variables, Eq. (11) is equivalent to the d'Alembert-type equation

$$\begin{aligned}&\left[-(1-a)\, \frac{\partial}{\rho\, \partial\rho}\, \frac{\rho\, \partial}{\partial\rho} + a\, \partial_s^2\right]\, \Phi^{(1)}(a, k; \rho, s) \\ &\qquad = g(k; \rho, s)\,,\end{aligned} \tag{12}$$

where the r.h.s. is the Green function $g(k; \boldsymbol{r}_1, \boldsymbol{r}_2)$ also expressed in terms of the coordinates $\boldsymbol{R}$.
The above d'Alembert equation can be solved in the Fourier domain and closed-form can be obtained to all orders in the expansion of $\Phi^{(1)}$ in powers of k, by using methods similar to those in evaluating Feynman diagrams. The function $\Phi^{(1)}$ is only defined up to a solution of the homogeneous d'Alembert equation – a non-uniqueness which can be utilized in choosing a solution which behaves smoothly in the limit of parallel planes, $a \to 0$.
- Further, it can be shown that the expansion of $\Phi^{(1)}$ in powers of k has the form

$$\begin{aligned}&\Phi^{(1)}(a, k; \boldsymbol{r}_1(\boldsymbol{R}), \boldsymbol{r}_2(\boldsymbol{R})) \equiv \widehat{\Phi}^{(1)}(a, k; \rho, s) \\ &= -\frac{1}{8\pi\, (1-a)^{1/2}} \sum_{n=0}^{\infty} \frac{(\mathrm{i}\, k)^n}{(n+1)!}\, (\rho^2 + s^2)^{(n+1)/2} \\ &\qquad\qquad \Phi_n^{(1)}\left(a, \frac{s^2}{\rho^2 + s^2}\right),\end{aligned} \tag{13}$$

with closed-form coefficient functions Φ_n dependent only on a and a single variable $\sigma := s^2/(\rho^2 + s^2)$. In particular, the lowest-order term in the expansions is

$$\begin{aligned}&\Phi_0^{(1)}(a, \sigma) \\ &= 2\,\mathrm{Re}\left\{\sqrt{1-a} - \sqrt{\sigma - a} + \tfrac{1}{2}\, \sqrt{1-a}\, \sqrt{\sigma}\, \ln \lambda(a, \sigma)\right\},\end{aligned} \tag{14}$$

where

$$\lambda(a,\sigma) := \frac{\sqrt{(1-a)\,\sigma}+\sqrt{\sigma-a}}{\sqrt{(1-a)\,\sigma}-\sqrt{\sigma-a}}\,\frac{1-\sqrt{\sigma}}{1+\sqrt{\sigma}}\,. \qquad (15)$$

The above representation allows one to convert the surface integral $\int \mathrm{d}S_1\,\mathrm{d}S_2\;1/|\boldsymbol{R}_1-\boldsymbol{R}_2|$ to line integrals involving a smoothly behaved integrand (as in Eq. (6)).

III. Conversion of the surface to line integrals in matrix elements of the vector Green function

The solutions for the functions $\Phi(1)$ and $\Phi(2)$ can be used in the evaluation of matrix elements of the vector Green function with RWG trial and testing functions. Such a matrix element is a sum of integrals

$$\begin{aligned} &A_{1,2}(a,k) \qquad (16)\\ &= \int_{T_1}\mathrm{d}S_1\int_{T_2}\mathrm{d}S_2\;\boldsymbol{\Psi}_1(\boldsymbol{R}_1)\cdot[\,\boldsymbol{g}(k,\boldsymbol{R}_1-\boldsymbol{R}_2)\times\boldsymbol{\Psi}_2(\boldsymbol{R}_2)]\\ &= \int_{T_1}\mathrm{d}S_1\int_{T_2}\mathrm{d}S_2\;[\boldsymbol{\Psi}_1(\boldsymbol{R}_1)\times\boldsymbol{\Psi}_2(\boldsymbol{R}_2)]\cdot\boldsymbol{g}(k,\boldsymbol{R}_1-\boldsymbol{R}_2)\,, \end{aligned}$$

where $\boldsymbol{\Psi}_i$ are RWG "half-basis functions" supported on single triangles and where $\boldsymbol{g}(k,\boldsymbol{R}) = \boldsymbol{\nabla}_{\boldsymbol{R}}\,g(k,|\boldsymbol{R}|)$ is the gradient of the Helmholtz-equation Green function (1).

We now outline the procedure of converting the integral (16) to a line integral over the triangles' perimeters; to achieve this goal, we need to solve generalizations of the d'Alembert equation (11) to the gradient of the Green function and to the "bi-d'Alembert" equation, i.e.,

$$\left\{\boldsymbol{\nabla}_{\boldsymbol{r}_1}\cdot[\hat{M}_a\,\boldsymbol{\nabla}_{\boldsymbol{r}_2}]\right\}\boldsymbol{\Phi}^{(1)}(a,k;\boldsymbol{r}_1,\boldsymbol{r}_2) = \boldsymbol{g}(k;\boldsymbol{r}_1,\boldsymbol{r}_2)\,, \quad (17a)$$

and

$$\left\{\boldsymbol{\nabla}_{\boldsymbol{r}_1}\cdot[\hat{M}_a\,\boldsymbol{\nabla}_{\boldsymbol{r}_2}]\right\}^2\boldsymbol{\Phi}^{(2)}(a,k;\boldsymbol{r}_1,\boldsymbol{r}_2) = \boldsymbol{g}(k;\boldsymbol{r}_1,\boldsymbol{r}_2)\,, \quad (17b)$$

hence

$$\boldsymbol{\nabla}_{\boldsymbol{r}_1}\cdot[\hat{M}_a\,\boldsymbol{\nabla}_{\boldsymbol{r}_2}]\,\boldsymbol{\Phi}^{(2)}(a,k;\boldsymbol{r}_1,\boldsymbol{r}_2) = \boldsymbol{\Phi}^{(1)}(a,k;\boldsymbol{r}_1,\boldsymbol{r}_2)\,. \quad (18)$$

We need here vector-valued functions $\boldsymbol{\Phi}$ simply because the matrix element (16) involves the gradient $\boldsymbol{g}$ of the Helmholtz-equation Green function. The reason we need a "second-order" function $\boldsymbol{\Phi}^{(2)}$ satisfying the an equation with the square of the d'Alembert operator is that our basis functions are linear functions of the (local) coordinates and we have to integrate by parts *twice*, to first reduce them to constants and then to delta functions at their boundaries. Evidently, such a procedure can be generalized to arbitrary polynomial basis functions.

By expressing the global coordinates $\boldsymbol{R}_i$ in terms of the local coordinates $\boldsymbol{r}_i$, by using the representation (17a), and by integration by parts, we can write Eq. (16) as

$$\begin{aligned} &A_{1,2}(a,k)\\ &= \int_{T_1}\mathrm{d}^2r_1\int_{T_2}\mathrm{d}^2r_2\;[\boldsymbol{\Psi}_1(\boldsymbol{R}_1(\boldsymbol{r}_1))\times\boldsymbol{\Psi}_2(\boldsymbol{R}_2(\boldsymbol{r}_1))]\\ &\qquad\cdot\left\{\boldsymbol{\nabla}_{\boldsymbol{r}_1}\cdot[\hat{M}_a\,\boldsymbol{\nabla}_{\boldsymbol{r}_2}]\right\}\boldsymbol{\Phi}^{(1)}(a,k;\boldsymbol{r}_1,\boldsymbol{r}_2)\\ &= \int_{T_1}\mathrm{d}^2r_1\int_{T_2}\mathrm{d}^2r_2\;\boldsymbol{\Phi}^{(1)}(a,k;\boldsymbol{r}_1,\boldsymbol{r}_2) \qquad (19)\\ &\qquad\cdot\left\{\boldsymbol{\nabla}_{\boldsymbol{r}_1}\cdot[\hat{M}_a\,\boldsymbol{\nabla}_{\boldsymbol{r}_2}]\right\}[\boldsymbol{\Psi}_1(\boldsymbol{R}_1(\boldsymbol{r}_1))\times\boldsymbol{\Psi}_2(\boldsymbol{R}_2(\boldsymbol{r}_1))]\,. \end{aligned}$$

Since the basis functions $\boldsymbol{\Psi}_i$ are linear in $\boldsymbol{r}_i$, the d'Alembert operator acting on their product yield terms proportional to a constant, as well as terms proportional to the delta functions supported on the boundaries ∂T_i of the triangles; we denote these functions by $\delta_i(\boldsymbol{r}_i)$.

The constant term – a certain vector $\boldsymbol{V}_{1,2}$ – gives rise, initially, to a surface integral. It is then converted to a line integral by expressing the first-order function $\boldsymbol{\Phi}^{(1)}$ in terms of the second-order one (Eq. (18)),

$$\begin{aligned} &\int_{T_1}\mathrm{d}^2r_1\int_{T_2}\mathrm{d}^2r_2\;\boldsymbol{\Phi}^{(1)}(a,k;\boldsymbol{r}_1,\boldsymbol{r}_2)\cdot\boldsymbol{V}_{1,2}\\ &= \int_{T_1}\mathrm{d}^2r_1\int_{T_2}\mathrm{d}^2r_2\;\left\{\boldsymbol{\nabla}_{\boldsymbol{r}_1}\cdot[\hat{M}_a\,\boldsymbol{\nabla}_{\boldsymbol{r}_2}]\right\}\boldsymbol{\Phi}^{(2)}(a,k;\boldsymbol{r}_1,\boldsymbol{r}_2)\cdot\boldsymbol{V}_{1,2}\\ &= \oint_{\partial T_1}\mathrm{d}l_1(\boldsymbol{r}_1)\oint_{\partial T_2}\mathrm{d}l_2(\boldsymbol{r}_2)\left\{\hat{\boldsymbol{u}}_1(\boldsymbol{r}_1)\cdot[\,\hat{M}\,\boldsymbol{u}_2(\boldsymbol{r}_2)]\right\}\\ &\qquad\boldsymbol{\Phi}^{(2)}(a,k;\boldsymbol{r}_1,\boldsymbol{r}_2)\cdot\boldsymbol{V}_{1,2}\,. \qquad (20) \end{aligned}$$

The term proportional to the product of the delta functions δ_1 and δ_2 results in the integral of the form

$$\begin{aligned} &\int_{T_1}\mathrm{d}^2r_1\int_{T_2}\mathrm{d}^2r_2\;\boldsymbol{\Phi}^{(1)}(a,k;\boldsymbol{r}_1,\boldsymbol{r}_2)\cdot\boldsymbol{U}_{1,2}(\boldsymbol{r}_1,\boldsymbol{r}_2)\\ &\qquad\delta_1(\boldsymbol{r}_1)\,\delta_2(\boldsymbol{r}_2) \qquad (21)\\ &= \oint_{\partial T_1}\mathrm{d}l_1(\boldsymbol{r}_1)\oint_{\partial T_2}\mathrm{d}l_2(\boldsymbol{r}_2)\;\boldsymbol{\Phi}^{(1)}(a,k;\boldsymbol{r}_1,\boldsymbol{r}_2)\cdot\boldsymbol{U}_{1,2}(\boldsymbol{r}_1,\boldsymbol{r}_2)\,, \end{aligned}$$

i.e., a line integral with a certain function $\boldsymbol{U}_{1,2}$ linear in its arguments.

Finally, terms proportional to single delta function, δ_1 or δ_2, result in line integrals of derivatives of the function $\boldsymbol{\Phi}^{(2)}$. For instance, the term proportional to δ_1 gives rise to

$$\begin{aligned} &\int_{T_1}\mathrm{d}^2r_1\int_{T_2}\mathrm{d}^2r_2\;\boldsymbol{L}_1(\boldsymbol{r}_1,\boldsymbol{r}_2)\,\delta_1(\boldsymbol{r}_1)\cdot\boldsymbol{\Phi}^{(1)}(a,k;\boldsymbol{r}_1,\boldsymbol{r}_2)\\ &= \oint_{\partial T_1}\mathrm{d}l_1(\boldsymbol{r}_1)\int_{T_2}\mathrm{d}^2r_2\;\boldsymbol{L}_1(\boldsymbol{r}_1,\boldsymbol{r}_2)\cdot\boldsymbol{\Phi}^{(1)}(a,k;\boldsymbol{r}_1,\boldsymbol{r}_2)\\ &= \oint_{\partial T_1}\mathrm{d}l_1(\boldsymbol{r}_1)\int_{T_2}\mathrm{d}^2r_2\;\boldsymbol{L}_1(\boldsymbol{r}_1,\boldsymbol{r}_2)\cdot\left\{\boldsymbol{\nabla}_{\boldsymbol{r}_1}\cdot[\hat{M}_a\,\boldsymbol{\nabla}_{\boldsymbol{r}_2}]\right\}\\ &\qquad\boldsymbol{\Phi}^{(2)}(a,k;\boldsymbol{r}_1,\boldsymbol{r}_2)\\ &= -\oint_{\partial T_1}\mathrm{d}l_1(\boldsymbol{r}_1)\oint_{\partial T_2}\mathrm{d}l_2(\boldsymbol{r}_2)\;\boldsymbol{L}_1(\boldsymbol{r}_1,\boldsymbol{r}_2)\cdot \qquad (22)\\ &\qquad\left\{\boldsymbol{\nabla}_{\boldsymbol{r}_1}\,\boldsymbol{\Phi}^{(2)}(a,k;\boldsymbol{r}_1,\boldsymbol{r}_2)\cdot\,[\hat{M}_a\,\hat{\boldsymbol{u}}(\boldsymbol{r}_2)]\right\}, \end{aligned}$$

where we have used the relation (18) and where $\boldsymbol{L}_1(\boldsymbol{r}_1,\boldsymbol{r}_2)$ is a certain function linear in its arguments.

Eqs. (20), (21), and (22) show that, indeed, all the surface integrals in the matrix element (16) reduce to line integrals of the auxiliary functions $\boldsymbol{\Phi}^{(1)}$ and $\boldsymbol{\Phi}^{(2)}$, as well as their derivatives. As before, these functions can be also obtained in a closed form, to all orders in k, by using Fourier-space and Feynman-diagram techniques.

In particular, $\boldsymbol{\Phi}^{(1)}$ can be evaluated as a gradient of the previous function $\Phi^{(1)}$. With $R=\sqrt{\rho^2+s^2}$, gradients of the

terms in the expansion (13) are given by

$$\begin{aligned}&\boldsymbol{\nabla}_{\boldsymbol{\rho},s}\left\{R^{n+1}\,\Phi_n^{(1)}(a,\sigma)\right\}\\&=(n+1)\,R^n\begin{bmatrix}\sqrt{1-\sigma}\,\hat{\boldsymbol{\rho}}\\ \pm\sqrt{\sigma}\end{bmatrix}\Phi_n^{(1)}(a,\sigma)\\&\quad+2\,R^n\begin{bmatrix}-\hat{\boldsymbol{\rho}}\\ \pm 1\end{bmatrix}\sqrt{\sigma}\,(1-\sigma)\,\partial_\sigma\,\Phi_n^{(1)}(a,\sigma)\,,\end{aligned}\tag{23}$$

where the $n=0$ contribution is

$$\begin{aligned}&\sqrt{\sigma}\,(1-\sigma)\,\partial_\sigma\,\Phi_0^{(1)}(a,\sigma)\\&=\mathrm{Re}\left\{-\sqrt{\sigma}\left(\sqrt{1-a}-\sqrt{\sigma-a}\right)\right.\\&\qquad\left.+\tfrac{1}{2}\sqrt{1-a}\,(1-\sigma)\,\ln\lambda(a,\sigma)\right\},\end{aligned}\tag{24}$$

with the previously defined function (15).

The second-order vector-valued function $\boldsymbol{\Phi}^{(2)}$ is given by the gradient of an expansion analogous to Eq. (13),

$$\begin{aligned}&\widehat{\boldsymbol{\Phi}}^{(2)}(a,k;\boldsymbol{\rho},s)=\boldsymbol{\nabla}_{\boldsymbol{\rho},Z}\,\widehat{\Phi}^{(2)}(a,k;\rho,s)\\&=\frac{1}{16\,\pi\,(1-a)^{3/2}}\sum_{n=0}^{\infty}\frac{(\mathrm{i}\,k)^n}{(n+1)!\,(n+3)}\\&\quad\boldsymbol{\nabla}_{\boldsymbol{\rho},s}\left\{(\rho^2+s^2)^{n/2+3/2}\,\Phi_n^{(2)}\left(a,\frac{s^2}{\rho^2+s^2}\right)\right\}.\end{aligned}\tag{25}$$

The lowest order contribution is

$$\begin{aligned}\boldsymbol{\nabla}_{\boldsymbol{\rho},s}\left\{R^3\,\Phi_0^{(2)}(a,\sigma)\right\}&=3\,R^2\begin{bmatrix}\sqrt{1-\sigma}\,\hat{\boldsymbol{\rho}}\\ \pm\sqrt{\sigma}\end{bmatrix}\Phi_0^{(2)}(a,\sigma)\\&\quad+2\,R^2\begin{bmatrix}-\hat{\boldsymbol{\rho}}\\ \pm 1\end{bmatrix}\sqrt{\sigma}\,(1-\sigma)\,\partial_\sigma\,\Phi_0^{(2)}(a,\sigma)\,,\end{aligned}\tag{26}$$

where the scalar second-order coefficient function $\Phi_0^{(2)}$ and its derivative are given by

$$\begin{aligned}\Phi_0^{(2)}(a,\sigma)&=2\,\mathrm{Re}\left\{\frac{(1-a)^{3/2}}{6}\,(4-15\,\sigma)\right.\\&\quad-\frac{(\sigma-a)^{1/2}}{6}\left[2\,(3-10\,\sigma)-a\,(4-15\,\sigma)\right]\\&\quad\left.-\frac{(\sigma-a)^{1/2}\,\sigma}{2\,a}+\frac{(1-a)^{3/2}\,(3-5\,\sigma)\,\sigma^{1/2}}{4}\,\ln\lambda(a,\sigma)\right\}\end{aligned}\tag{27}$$

and

$$\begin{aligned}\sqrt{\sigma}\,(1-\sigma)\,\partial_\sigma\,\Phi_0^{(2)}(a,\sigma)&=\mathrm{Re}\left\{-\sqrt{\sigma}\left(\sqrt{1-a}-\sqrt{\sigma-a}\right)\right.\\&\quad\left.+\tfrac{1}{2}\sqrt{1-a}\,(1-\sigma)\,\ln\lambda(a,\sigma)\right\}.\end{aligned}\tag{28}$$

IV. Conversion of the surface to line integrals in matrix elements of the tensor Green function

Since this problem can be handled similarly to the case of the vector Green function, we only briefly sketch the main steps. In the notation analogous to Eq. (16), a matrix element of the tensor Green function (the electric-field operator) is a sum of two terms:

(i) The "electrostatic" contribution involving the scalar Green function g and surface divergences surface divergences $\boldsymbol{\nabla}_{\boldsymbol{R}_i}\cdot\boldsymbol{\Psi}_i(\boldsymbol{R}_i)$ of the basis functions. For RWG basis functions these divergences are constants, hence the considered term can be converted to line integrals by using the basic representation (4) or (11).

(ii) The "magnetic-potential" contribution involving the Green function g and the dot-product $\boldsymbol{\Psi}_1(\boldsymbol{R}_1)\cdot\boldsymbol{\Psi}_2(\boldsymbol{R}_2)$ of the basis functions. By using the representation (11) and integrating by parts, one obtains a suface integral of $\Phi^{(1)}$ and the product of the basis functions (a bilinear function of the coordinates) acted upon by the d'Alembert operator; the latter quantity is a constant.[1] This surface integral is then reduced to a line integral by expressing $\Phi^{(1)}$ in terms of a scalar second-order function $\Phi^{(2)}$ (defined as in Eq. (18)) and integrating once more by parts.

V. Analytic evaluation of the line integrals

We sketch here a procedure which leads, eventually, to analytic evaluation of the matrix elements.

Our final expressions for matrix elements are double line integrals over pairs of edges belonging to the considered two triangles T_1 and T_2; schematically,

$$\begin{aligned}A_{12}=\sum_{i,j=1,3}B_{i,j}\int\mathrm{d}l_i(\boldsymbol{R}_1)\int\mathrm{d}l_j(\boldsymbol{R}_2)\\\widehat{\Phi}(a,k,\rho(\boldsymbol{R}_1-\boldsymbol{R}_2),s(\boldsymbol{R}_1-\boldsymbol{R}_2))\,,\end{aligned}\tag{29}$$

where $B_{i,j}$ are constant coefficients and $\widehat{\Phi}$ is an expression similar to Eq. (13), i.e., a function of the variables

$$\rho=\sqrt{[\hat{\boldsymbol{X}}\cdot(\boldsymbol{R}_1-\boldsymbol{R}_2)]^2+[\hat{\boldsymbol{Y}}\cdot(\boldsymbol{R}_1-\boldsymbol{R}_2)]^2}\tag{30a}$$

and

$$s=\hat{\boldsymbol{Z}}\cdot(\boldsymbol{R}_1-\boldsymbol{R}_2)\,.\tag{30b}$$

In evaluating the line integrals, we parameterize the coordinates of the integration points on the edges as linear functions $\boldsymbol{R}_1(\xi_1)$ and $\boldsymbol{R}_2(\xi_2)$ of two normalized length parameters $\xi_1,\xi_2\in[0,1]$. It follows that s is a linear function of the variables ξ_1, ξ_2, and ρ^2 is a quadratic function, say

$$s(\boldsymbol{R}_1(\xi_1)-\boldsymbol{R}_2(\xi_2))=L_0(\xi_1,\xi_2)=a_0+b_1\,\xi_1+b_2\,\xi_2\tag{31a}$$

and

$$\begin{aligned}&\rho^2(\boldsymbol{R}_1(\xi_1)-\boldsymbol{R}_2(\xi_2))=Q_0(\xi_1,\xi_2)\\&=A_0+B_1\,\xi_1+B_2\,\xi_2+C_1\,\xi_1^2+C_2\,\xi_2^2+C_{12}\,\xi_1\,\xi_2\,.\end{aligned}\tag{31b}$$

The most general form of an integrand in Eq. (29) (exemplified by Eqs. (13), (23), (25), and (26) with the explicit formulae Eqs. (14), (24), (27), and (28)) is a sum of terms of two types:

(i) A polynomial in expressions $\sqrt{A\,\rho^2+B\,s^2}$ (with some constants A and B), i.e., a polynomial in $\sqrt{Q(\xi_1,\xi_2)}$, where Q is some quadratic form.

[1] More precisely, a constant plus delta-functions on the boundaries of the triangles. The resulting additionl contributions, analogous to Eq. (22), are expressible in terms of gradients of the functions $\Phi^{(i)}$.

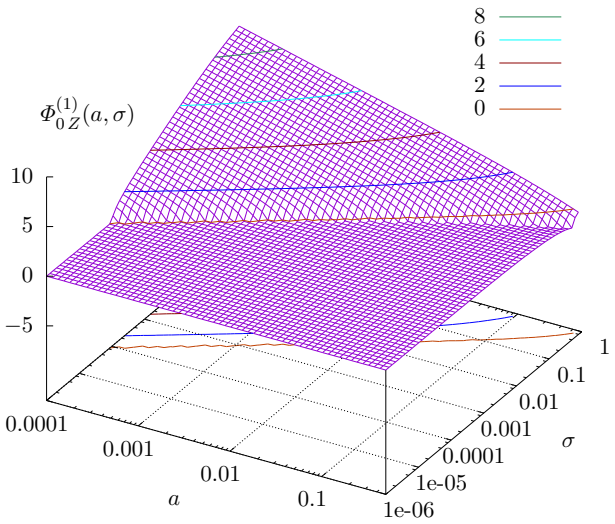

Fig. 2: The Z component of the zero-th order auxiliary function $\boldsymbol{\Phi}_0^{(1)}$, plotted in logarithmic scales of its arguments in order to emphasize the regions of small a and small σ.

(ii) A polynomial in ρ^2, s^2, and s (without the square-root) multiplying the logarithm of the function λ of Eq. (15). As a function of ρ and s, λ is given by

$$\lambda = \frac{\sqrt{1-a}\,s + \sqrt{(1-a)\,s^2 - a\rho^2}}{\sqrt{1-a}\,s - \sqrt{(1-a)\,s^2 - a\rho^2}} \frac{\sqrt{s^2+\rho^2} - s}{\sqrt{s^2+\rho^2} + s}\,; \quad (32)$$

hence, all terms of the type (ii) have the general form $P(\xi_1,\xi_2)\ \ln\big(L(\xi_1,\xi_2) + \sqrt{Q(\xi_1,\xi_2)}\,\big)$, where P is a polynomial, L a linear function, and Q a quadratic function.

The integrals $\int_0^1 \mathrm{d}\xi_1 \int_0^1 \mathrm{d}\xi_2 \cdots$ of the terms of the types (i) and (ii) can be obtained in a closed form and are expressible in terms of elementary functions.

VI. Representative Numerical Results

In analogy to Eq. (13), the auxiliary functions $\boldsymbol{\Phi}^{(1)}$ and $\boldsymbol{\Phi}^{(2)}$, given by Eqs. (17), can be also expanded in powers of k. Explicit closed-form expressions for the coefficients of the expansions, $\boldsymbol{\Phi}_n^{(1)}(a,\sigma)$ and $\boldsymbol{\Phi}_n^{(2)}(a,\sigma)$, show that these coefficients, as functions of σ, are bounded and piecewise continuously differentiable in the subintervals for $0 < \sigma < a$ and $a < \sigma < 1$. At the point $\sigma = a$ derivatives of the coefficient functions may be discontinuous, as seen, e.g., in Fig. 2.

The behavior of the functions $\boldsymbol{\Phi}^{(1)}$ and $\boldsymbol{\Phi}^{(2)}$ indicates that integration region in the line integrals (20) to (22) should be split into sub-domains in which derivatives of the integrand are bounded and thus conventional Gaussian quadratures quickly convergent.

A certain difficulty arises in the case when two edges of the triangles, one in T_1 and the other in T_2, share a vertex. In those cases the argument σ of the functions $\boldsymbol{\Phi}_n^{(1)}(a,\sigma)$ and $\boldsymbol{\Phi}_n^{(2)}(a,\sigma)$, although bounded in the interval $[0,1]$, has an indefinite $(0/0$-type) limit when the points $\boldsymbol{r}_1$ and $\boldsymbol{r}_2$ approach the common vertex. For such edges, however, the double line integral can be reduced to a single integral with a piecewise smooth integrand, which can be efficiently evaluated by standard quadratures.

In general, as will be discussed in the presentation, the proposed approach to evaluating matrix elements of the vector Green function has definite advantages – in terms of the accuracy versus the number of quadrature points – over presently available methods, in particular singularity subtraction techniques.

Acknowledgments

This material is based upon work supported by US Air Force Office of Scientific Research under award number FA955016C0014.

References

[1] E. H. Bleszynski, M. K. Bleszynski, and T. Jaroszewicz, "Reduction of singular surface integrals to nonsingular line integrals in integral equations for planar geometries," *IEEE Transactions on Antennas and Propagation*, vol. 64, no. 11, pp. 4760–4769, 2016.

[2] S. M. Rao, D. R. Wilton, and A. W. Glisson, "Electromagnetic scattering by surfaces of arbitrary shape," *IEEE Transactions on Antennas and Propagation*, vol. AP-30, pp. 409–418, 1982.

[3] A. Tzoulis and T. F. Eibert, "Review of singular potential integrals for method of moments solutions of surface integral equations," *Advances in Radio Science*, vol. 2, pp. 93–99, 2004.

[4] I. Hänninen, M. Taskinen, and J. Sarvas, "Singularity subtraction integral formulae for surface integral equations with RWG, rooftop and hybrid basis functions," *Progress in Electromagnetics Research*, vol. 63, pp. 243–278, 2006.

[5] M. G. Duffy, "Quadrature over a pyramid or cube of integrands with a singularity at a vertex," *SIAM Journal on Numerical Analysis*, vol. 19, no. 6, pp. 1260–1262, 1982.

[6] M. A. Khayat and D. R. Wilton, "Numerical evaluation of singular and near-singular potential integrals," *IEEE Transactions on Antennas and Propagation*, vol. 53, pp. 3180–3190, 2005.

[7] M. M. Botha, "A family of augmented Duffy transformations for near-singularity cancellation quadrature," *IEEE Transactions on Antennas and Propagation*, vol. 61, no. 6, pp. 3123–3134, 2013.

[8] E. Bleszynski, M. Bleszynski, and T. Jaroszewicz, "Reduction of singular surface integrals to non-singular line integrals in integral equations involving non-parallel surface elements," in *2017 11th European Conference on Antennas and Propagation (EUCAP)*. IEEE, 2017, pp. 303–307.

APPENDIX E (CEM'i 2018)

Non-singular Laplacian representations of singular kernels of electromagnetic integral equations

Elizabeth Bleszynski[1], Marek Bleszynski[1], and Thomas Jaroszewicz[1]

[1]*Monopole Research, Thousand Oaks, CA 91360, USA*

elizabeth@monopoleresearch.com

We consider extensions and selected applications of the recently proposed method of evaluating Galerkin matrix elements of electromagnetic volume and surface integral equations with the help of suitably constructed Laplacian-type representations of singular kernels (Green functions) in terms of non-singular auxiliary functions. Such representations allows us, by using the Gauss divergence theorem, to convert volumetric and surface integrals representing matrix elements to respective surface or line integrals always involving only non-singular integrands.

The task of finding specific Laplacian representations of various kernels amounts to solving appropriate ordinary or partial inhomogeneous differential equations. Simple solutions of resulting ordinary differential equations which pertain to volume and planar surface geometries are obtained in terms of elementary functions. In the case of basis functions supported on non-parallel surface elements, partial differential equations for the auxiliary functions are first solved in Fourier space and then transformed to simple expressions in coordinate space by evaluating integrals similar to those used in treating Feynman diagrams.

The most essential element of the procedure consisted of employing a Laplacian-type representation of the Green function of the scalar Helmholtz equation,

$$g(k,R)=\frac{\mathrm{e}^{\,\mathrm{i}\,kR}}{4\pi R}\,, \tag{1}$$

with k being the free-space wave number. The first representation of the Green function (1) in terms of an auxiliary, non-singular function $h(\xi)$ of a ***single argument*** $\xi=\mathrm{i}kR\equiv\mathrm{i}k\,|\boldsymbol{R}_1-\boldsymbol{R}_2|$, has the form [1]

$$g\big(k,|\boldsymbol{R}_1-\boldsymbol{R}_2|\big)=\frac{1}{4\pi\mathrm{i}k}(\boldsymbol{\nabla}_{\boldsymbol{R}_1}\cdot\boldsymbol{\nabla}_{\boldsymbol{R}_2})\,h(\mathrm{i}k\,|\boldsymbol{R}_1-\boldsymbol{R}_2|)\,. \tag{2}$$

This representation can be rewritten in the equivalent form of the second-order differential equation for the function $h(\xi)$

$$\frac{\partial^2}{\partial\xi^2}\,h(\xi)-\frac{2}{\xi}\,\frac{\partial}{\partial\xi}\,h(\xi)=\frac{\mathrm{e}^{\xi}}{\xi}\,,$$

which has the general solution $h(\xi)=\mathrm{e}^{\xi}/\xi+c_1+c_2/\xi$, where c_1 and c_2 are two arbitrary constants. With the specific choice of $c_1=c_2=-1$ we obtain a particular solution of the differential equation $h(\xi)=(\mathrm{e}^{\xi}-1-\xi)/\xi$ having a finite limit at $\xi=0$. Such a choice of $h(\xi)$ allows us to convert the 6-dimensional volume integrals over tetrahedrons to 4-dimensional surface integrals over the tetrahedra faces with nonsingular integrands,

$$\int\limits_{V_1}\mathrm{d}V_1\int\limits_{V_2}\mathrm{d}V_2\;g(k,|\boldsymbol{R}_1-\boldsymbol{R}_2|)=\frac{1}{4\pi\mathrm{i}k}\int\limits_{\partial V_1}\mathrm{d}S_1\int\limits_{\partial V_2}\mathrm{d}S_2\,(\hat{\boldsymbol{n}}_1\cdot\hat{\boldsymbol{n}}_2)\,h(\mathrm{i}k\,|\boldsymbol{R}_1-\boldsymbol{R}_2|)\,, \tag{3}$$

where ∂V_1 and ∂V_2 are the surfaces bounding tetrahedra volumes V_1 and V_2 and $\hat{\boldsymbol{n}}_1$ and $\hat{\boldsymbol{n}}_2$ are the outward pointing unit vectors perpendicular to the tetrahedra faces.

We have also obtained a second representation of the scalar Green function of the Helmholtz equation, applicable to conversion of surface integrals over two triangular facets $T_1\subset\Pi_1$ and $T_2\subset\Pi_1$, lying in two

non-parallel planes Π_1, Π_2, to line integrals over triangle perimeters. The representation involves a bilinear form of two gradient operators $\boldsymbol{\nabla}_1$ and $\boldsymbol{\nabla}_2$ acting in the planes Π_1 and Π_2. In analogy to Eq. (2), it has the form [2]

$$g\big(k, |\boldsymbol{R}_1 - \boldsymbol{R}_2|\big) = \big\{\boldsymbol{\nabla}_1 \cdot [\,\hat{M}_a\, \boldsymbol{\nabla}_2\,]\big\}\, \Phi^{(1)}(k, a, \boldsymbol{R}_1 - \boldsymbol{R}_2)\,, \tag{4}$$

where $\boldsymbol{\nabla}_1 = \hat{\boldsymbol{n}}_1 \times (\boldsymbol{\nabla}_{\boldsymbol{R}_1} \times \hat{\boldsymbol{n}}_1)$ and $\boldsymbol{\nabla}_2 = \hat{\boldsymbol{n}}_2 \times (\boldsymbol{\nabla}_{\boldsymbol{R}_2} \times \hat{\boldsymbol{n}}_2)$, $\hat{\boldsymbol{n}}_1 \neq \hat{\boldsymbol{n}}_2$ denote unit vectors perpendicular to triangle faces, and $\hat{M}_a = \mathrm{diag}(1, 1-a)$ is a (2×2) diagonal matrix dependent on the "inclination parameter" $a = \sin^2\theta \leq \frac{1}{2}$, where 2θ is the angle between the planes Π_1 and Π_2, i.e., $\hat{\boldsymbol{n}}_1 \cdot \hat{\boldsymbol{n}}_2 = \cos 2\theta$. The representation (4) of the Green function can be rewritten in the equivalent form of a second-order partial-differential equation in two spatial variables, $s = \hat{\boldsymbol{z}} \cdot (\boldsymbol{R}_1 - \boldsymbol{R}_2)$ (with $\hat{\boldsymbol{z}} \equiv (\hat{\boldsymbol{n}}_1 + \hat{\boldsymbol{n}}_2)/|\hat{\boldsymbol{n}}_1 + \hat{\boldsymbol{n}}_2|$) and $\rho = \sqrt{(\boldsymbol{R}_1 - \boldsymbol{R}_2)^2 - s^2}$,

$$\left[-(1-a)\,\frac{\partial}{\rho\,\partial\rho}\,\frac{\rho\,\partial}{\partial\rho} + a\,\partial_s^2\right]\, \Phi^{(1)}(a, k; \rho, s) = \, g(k; \sqrt{\rho^2 + s^2})\,, \tag{5}$$

where both the (nonsingular) auxiliary function $\Phi^{(1)}$ and the Green function g are expressed in terms of ρ and s.

We have found a closed-form of the above d'Alembert equation to all orders in the expansion of $\Phi^{(1)}$ in powers of k, by means similar to those used in evaluating Feynman diagrams.

The representation (4) allows us to convert double surface integrals of the scalar Green function (as well as integrals appearing in the matrix elements of the dyadic Green function sandwiched between two RWG basis functions) over the triangles T_1 and T_2 to line integrals over the triangles' perimeters,

$$\int\limits_{T_1} \mathrm{d}S_1 \int\limits_{T_2} \mathrm{d}S_2\; g(k, |\boldsymbol{R}_1 - \boldsymbol{R}_2|) = \oint\limits_{\partial T_1} \mathrm{d}l_1 \oint\limits_{\partial T_2} \mathrm{d}l_2\, \big\{\hat{\boldsymbol{u}}_1 \cdot [\,\hat{M}_a\, \hat{\boldsymbol{u}}_2]\big\}\; \Phi^{(1)}(k, a, \boldsymbol{R}_1 - \boldsymbol{R}_2) \tag{6}$$

with $\hat{\boldsymbol{u}}_1$ and $\hat{\boldsymbol{u}}_2$ representing unit vectors perpendicular to the perimeter lines, located in the planes Π_1 and Π_2.

An advantage of the derived expressions for matrix elements is their simplicity and easily controllable accuracy without the need of using special numerical treatments of singular behavior of kernels. Our method results in expressions for matrix elements given in terms of integrals with well-behaved integrands, amenable to conventional low order numerical quadratures, or simply in analytical forms given in forms of linear combination of elementary functions. An important, demonstrated property of our expressions is that they remain well behaved in all special geometrical configurations of practical interest, in particular for adjacent, nearly adjacent, parallel, and nearly parallel surface elements.

The proposed method is of practical interest in such particular applications of integral equations as, e.g., design of metamaterials of nanophotonic devices, which rely on collective resonant behavior of many elements of sizes comparable to or less than the wavelength. The existence of resonances unavoidably increases the condition number of the problems, which amplifies inaccuracies in the elements of the impedance matrix. Therefore, reliable modeling of such systems requires highly accurate evaluation of matrix elements of the pertinent operators. Further, engineering applications (e.g., of photonic devices) typically require iterative optimization of the structures; hence, fast computation of the impedance matrices becomes a crucial requirement.

Representative numerical examples illustrating the proposed method efficiency and accuracy will be discussed.

ACKNOWLEDGMENT

This material is based upon work supported by the U. S. Air Force Office of Scientific Research under award number FA 9550-16-C-0014.

REFERENCES

[1] E. H. Bleszynski, M. K. Bleszynski, and T. Jaroszewicz, "Reduction of volume integrals to nonsingular surface integrals for matrix elements of tensor and vector Green functions of Maxwell equations," *IEEE Transactions on Antennas and Propagation*, vol. 61, pp. 3642–3647, 2013.

[2] E. Bleszynski, M. Bleszynski, and T. Jaroszewicz, "Reduction of singular surface integrals to non-singular line integrals in integral equations involving non-parallel surface elements," in *2017 11th European Conference on Antennas and Propagation (EUCAP)*. IEEE, 2017, pp. 303–307.